Towards sector-based attribution using intra-city variations in satellite-based emission ratios between CO_2 and CO

Dien Wu[1], Junjie Liu[2,1], Paul O. Wennberg[1,3], Paul I. Palmer[2,4], Robert R. Nelson[2], Matthäus Kiel[2], and Annmarie Eldering[2]

[1]Division of Geological and Planetary Sciences, California Institute of Technology, Pasadena, USA
[2]Jet Propulsion Laboratory, California Institute of Technology, Pasadena, USA
[3]Division of Engineering and Applied Science, California Institute of Technology, Pasadena, USA
[4]School of GeoSciences, University of Edinburgh, Edinburgh, UK

Correspondence: Dien Wu (dienwu@caltech.edu)

Abstract. Carbon dioxide (CO_2) and air pollutants such as carbon monoxide (CO) are co-emitted by many combustion sources. Previous efforts have combined satellite-based observations of multiple tracers to calculate their emission ratio (ER) for inferring combustion efficiency at the regional to city scale. Very few studies have focused on combustion efficiency at the sub-city scale or related it to emission sectors using space-based observations. Several factors are important for deriving and interpreting spatially-resolved ERs from asynchronous satellite measurements including 1) variations in meteorological conditions given the mismatch in satellite overpass times, 2) differences in vertical sensitivity of the retrievals (i.e., averaging kernel profiles), 3) interferences from the biosphere and biomass burning, and 4) mismatch in the daytime variation of CO and CO_2 emissions. In this study, we extended an established emission estimate approach to arrive at spatially-resolved ERs based on retrieved column-averaged CO_2 (XCO_2) from the Snapshot Area Mapping (SAM) mode of the Orbiting Carbon Observatory-3 (OCO-3) and column-averaged CO from the TROPOspheric Monitoring Instrument (TROPOMI).

To evaluate the influence of the confounding factors listed above and further explain intra-urban variations in ERs, we leveraged a Lagrangian atmospheric transport model with an urban land cover classification dataset and reported ER_{CO} from the sounding level to the overpass- and city- level. We found that the difference in the overpass times and averaging kernels between OCO and TROPOMI strongly affect the estimated spatially-resolved ER_{CO}. Specifically, a time difference of > 3 hours typically led to dramatic changes in wind directions and urban plume shapes and thereby making the calculation of accurate sounding-specific ER_{CO} difficult. After removing such cases from consideration and applying a simple plume shift method when necessary to account for changes in wind direction and speed, we discovered significant contrasts in combustion efficiencies between 1) two megacities versus two industry-oriented cities and 2) different regions within a city, based on six nearly-coincident overpasses per city. Results suggest that ER_{CO} impacted by the industry in Los Angeles is slightly lower than the overall city-wide value (< 10 ppb-CO / ppm-CO_2). In contrast, ER_{CO} related to the heavy industry in Shanghai is much higher than Shanghai's city-mean and more aligned with city-means of the two industry-oriented Chinese cities (approaching 20 ppb-CO / ppm-CO_2). Although investigations based on a larger number of satellite overpasses are needed, our unique approach (without using sector-specific information from emission inventories) provides guidance for assessing combustion

efficiency within a city based on future satellite missions, such as those that will map column CO_2 and CO concentration simultaneously with high spatiotemporal resolutions.

1 Introduction

Home to more than half of the total global population, urban areas have been expanding, especially in Asia and Africa with an urbanization rate of 1.3% and 1.1% yr^{-1} between 2015 and 2020 (World Urbanization Prospects 2018). Urban regions are also responsible for a significant amount of anthropogenic emissions of greenhouse gases (GHG) and air pollutants into the atmosphere including carbon dioxide (CO_2), methane, carbon monoxide (CO), and nitrogen oxides (Duncan et al., 2016; Lin et al., 2018; Super et al., 2017; Plant et al., 2019). To monitor the abundance of a number of atmospheric species in a globally-consistent manner, satellite observations have become indispensable (Yokota et al., 2009; Crisp et al., 2012; Veefkind et al., 2012). For example, carbon-monitoring satellites such as the Orbiting Carbon Observatory-2 (OCO-2, Crisp et al., 2012) have made the quantification of city-scale CO_2 emissions and emission trends possible (e.g., Hedelius et al., 2018; Ye et al., 2020; Wu et al., 2020; Shekhar et al., 2020; Lei et al., 2021). Quantifying the spatial gradient of atmospheric concentrations and relating the gradient to emissions within the city domain becomes the next critical yet challenging task. Understanding such spatial heterogeneity in emissions and the environmental consequences can support better decisions in urban planning and pinpointing hotspots for emission mitigation.

Given the co-benefit between GHG reduction and improved air quality at various scales (Zhang et al., 2017), controlling the consumption of fossil fuels altogether is the key. Efficiency associated with various combustion activities is linked to the underlying processes and conditions (e.g., oxygen-to-fuel ratio and temperature). For example, the amount of CO_2 emitted from coal-fired power plants varies with thermal and pressure conditions, the type of fuel consumed, the technology deployed, and the service duration of power plants (Yuan and Smith, 2011). Modern power generation with distinct scrubbing technology are often regarded as "clean" emitters leading to minimal CO and NO_x enhancements (Lindenmaier et al., 2014). The commonly-used approach in estimating combustion efficiency is to combine atmospheric observations of multiple trace gases and report the ratio of the total or excess measured concentrations (above a defined background value) between tracers (Silva and Arellano, 2017; Reuter et al., 2019; Park et al., 2021). Such tracer-to-tracer ratio calculation has the benefit that errors in describing the atmospheric transport that carries tracers to the measurement site can be cancelled. A few notable studies further utilized derived emission ratios (ERs) from ground or airborne measurements to infer sector-specific emission signals (Wennberg et al., 2012; Lindenmaier et al., 2014; Nathan et al., 2018; Tang et al., 2020).

CO and NO_x often serve as tracers for anthropogenic CO_2 due to their common sources (e.g., Palmer et al., 2006; Wunch et al., 2009; Hedelius et al., 2018). Analyzing remotely-sensed NO_x plumes with relatively short lifetime can help identify local fossil fuel CO_2 ($FFCO_2$) sources that would otherwise be difficult to detect (Reuter et al., 2019; Fujinawa et al., 2021). While at the same time, such reactivity raises the requirement of accurately accounting for chemical transformation and complicates the interpretation of emission signals or ERs from NO_x observations (Lama et al., 2020; Hakkarainen et al., 2021). Given its much longer lifetime, CO is much easier to interpret and more likely to be found during incomplete combustion. The emission ratio of CO to CO_2 (ER_{CO}) is usually estimated from sparse ground-based measurements within a city (Bares et al., 2018; Chandra et al., 2016; Lindenmaier et al., 2014) and from satellites at the city scale (Park et al., 2021; Silva and Arellano, 2017). Sector-specific activities and ER_{CO} such as from the traffic sector have been analyzed by limited but valuable tunnel studies (Ammoura et al., 2014; Bradley et al., 2000; Popa et al., 2014).

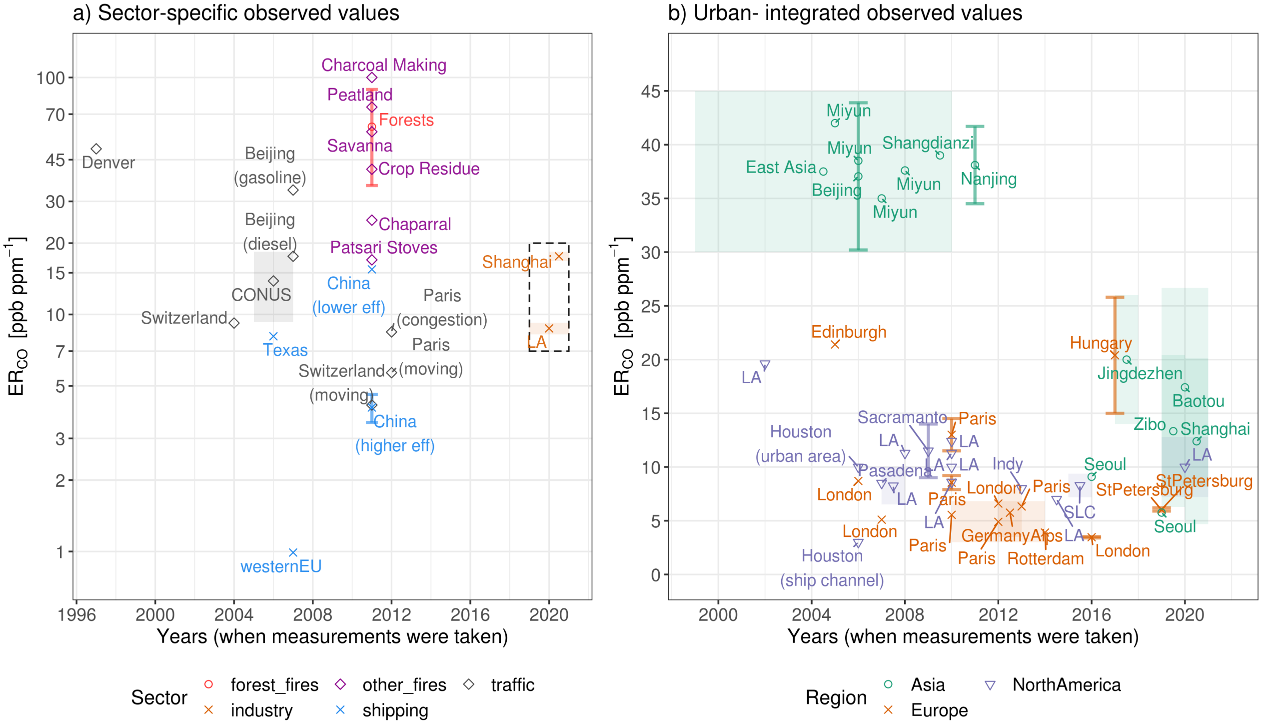

Figure 1. ER_{CO} [ppb ppm^{-1}] associated with specific processes (a) and ER_{CO} integrated over the entire city/region (b) summarized from previous studies. The x-axis indicates the time these estimates were made except for Akagi et al. (2011). 2011 was simply chosen for x-axis since the paper was published in 2011. The error bars represent the uncertainties in estimated ERs and transparent rectangle indicates the range of ERs over multiple years. Paper citations are omitted from the figure but included in **Appendix A**. ERs related to biomass burning and shipping sectors are derived using EF_{CO} and EF_{CO_2}. The range of overpass-specific ER_{CO} estimates for Shanghai, LA, Baotou, and Zibo derived from our study are added to the figure (dashed black box).

We performed a literature search on ER_{CO} derived from observations (**Appendix A**) and summarized the values in **Fig. 1**. Combustion efficiency fluctuates 1) over time (e.g., Turnbull et al., 2011b), likely explained by technological improvements and 2) between sub-sectors, e.g., gasoline vs. diesel vehicles or moving vs. congestion traffic (Westerdahl et al., 2009; Popa et al., 2014). Despite differences in measurement platforms and analysis approaches, the observed urban-integrated ER_{CO} values, especially for those in Europe and the United States, are well constrained within the range of 4 to 15 ppb ppm^{-1}(**Fig. 1b**). ER_{CO} for biomass burning and shipping sectors are estimated based on fuel-specific emission factors, i.e., ER_{CO} (= EF_{CO} / EF_{CO_2}) with proper unit conversions, where emission factor EF_X indicates the emission of gas X per kg of fuel burned.

When estimating fossil fuel emissions from a bottom-up perspective, most inventories rely on activity data and may involve prior knowledge of emission factors (Gurney et al., 2019; Solazzo et al., 2021). One notable example is Hestia, a high-resolution inventory for the US, which estimates CO_2 emissions of non-point sources based up CO emissions from the National Emission Inventory with EFs and carefully evaluates their adopted EFs (Gurney et al., 2019). However, when constructing emission inventories across regions/nations, the large variability in ERs across combustion processes, sectors, years, and regions (as seen in **Fig. 1a**) makes the choice of EFs extremely challenging. Accurate bottom-up emission estimates require accurate activity data and EF_X that naturally vary with combustion conditions (e.g., temperature, fuel load, oxygen level) and are generally not well known especially over data-scarce regions. To our knowledge, only a few global inventories, such as the Emissions Database for Global Atmospheric Research (EDGAR, Solazzo et al., 2021), offer global anthropogenic CO and CO_2 emissions. Considering the challenge in approximating ERs, certain knowledge derived from atmospheric observations may 1) complement inventory-based ERs (e.g., CO:NO_x ratio in Lama et al., 2020) and 2) facilitate the emission constraint for a desired gas usually with relatively larger uncertainties (Wunch et al., 2009; Palmer et al., 2006; Wang et al., 2009; Brioude et al., 2012; Nathan et al., 2018). Such prior achievements motivate us to examine ERs using satellite observations of multiple tracers.

Most existing studies focused on quantifying an integrated ER for the whole city or region. We take a step forward to zoom into an urban area and leverage spatially-resolved satellite observations. Intra-city variations in the satellite-based concentration of a specific air pollutant like NO_x have been analyzed and linked to societal inequalities regarding the income and educational attainment (Demetillo et al., 2021; Kerr et al., 2021). Yet, no one has attempted to study the intra-urban gradient in combustion efficiency from space and relate such a gradient to a specific combustion sector. This is now possible by virtue of the Orbiting Carbon Observatory-3 (OCO-3) mounted on the International Space Station that can sample a city-landscape during the Snapshot Area Mapping (SAM) mode (Eldering et al., 2019; Taylor et al., 2020; Kiel et al., 2021). In an effort to arrive at spatially-varying ERs from sensors with asynchronous orbits, we must account for several factors that have not been thoroughly investigated. These include 1) variations in meteorological conditions and emission patterns during different overpass times, 2) discrepancies in the vertical sensitivity of the retrievals (i.e., averaging kernel or AK profiles), and 3) interference from non-anthropogenic sources and sinks, especially from the biosphere.

In this study, we explore the spatial distribution of ER_{CO} within four urban areas mainly using XCO_2 observations from OCO-3 and XCO observations from the TROPOspheric Monitoring Instrument on board the Sentinel-5 Precursor (TROPOMI; Veefkind et al., 2012). To avoid relying on prior sector-specific information of ER_{CO} from emission inventories, we adopt the urban land cover data from high-resolution World Urban Database and Access Portal Tools (WUDAPT; Ching et al., 2018). WUDAPT offers the so-called Local Climate Zone (LCZ) that takes into account of the building structure/spacing along with vegetation coverage (Stewart and Oke, 2012), which shed light on the urban infrastructure.

Our work seeks to answer the following two questions.

1. Is it possible to accurately quantify spatially-resolved ER_{CO} from asynchronous satellite measurements?
2. Can the combustion efficiency for a given sector be determined without using prior emission inventories?

In Sect. 2, we describe the satellite data and methodology for obtaining emissions, ER_{CO}, and associated uncertainties. In Sect. 3, we show intra-city variations in ER_{CO} (including ER_{CO} tied to heavy industry in a megacity) and how multiple factors may interfere in deriving ER_{CO} . In Sect. 4, we discuss implications and limitations of this analysis.

2 Data and methodology

We targeted two types of cities: 1) industry- and energy- oriented cities (Baotou, China and Zibo, China), and 2) megacities with more diverse emission sectors (Shanghai, China and Los Angeles, US). The four cities are selected considering the amount and quality of XCO_2 data from OCO-3 SAMs and TROPOMI XCO data. The two industry- and energy- oriented cities in China are selected given their large amount of metal production plants for aluminum or iron and steel (Global Energy Infrastructure Emission Database, GID; Wang et al., 2019) and surrounding coal-fired power plants (Global Energy Monitor, GEM; and the Global Power Plant Dataset; World Resources Institute, WRI, 2018) that support the nearby industries.

Our goal is to calculate ER_{CO} from every satellite sounding within an urban plume that is a downwind area affected by urban emissions (**Sect. 2.2**). Sounding-dependent ER_{CO} are calculated as ratios of CO emissions over CO_2 emissions (**Eq. 3**) that are estimated from satellite-derived fossil fuel (FF) enhancements and further refined with a "scaling factor" in **Eq. 1**. This scaling factor accounts for several mismatches between OCO-2/3 and TROPOMI (**Sect. 2.1**) and is obtained from an atmospheric transport model (**Sect. 2.2.1**). Since we do not differentiate emission signals due to biofuel or fossil fuel combustion, the term "FF enhancement" is simply referred to as *column enhancement induced by any anthropogenic combustion processes by the target city*. Determination of FF enhancements requires an estimate of the background values (**Sect. 2.2.2**) and "second-order" correction terms for biogenic and pyrogenic sources (**Sect. 2.2.3**). Sounding-specific ERs and uncertainties (**Sect. 2.2.4**) are aggregated to yield an ER per overpass and per city. Lastly, we illustrate how ER_{CO} associated with heavy industry in Los Angeles and Shanghai can be extracted with the assistance of WUDAPT (**Sect. 2.3**).

2.1 Satellite observations and data pre-processing

We evaluated all overpasses coincidences between OCO-3 SAM and TROPOMI observations but only selected those with relatively small differences in overpass times. Considering the limited number of coincidences between sensors, two non-SAM overpasses from OCO-3 and one OCO-2 overpass are added to the analysis. As a result, six OCO-TROPOMI coincidences with higher data quality from Oct 2019 to June 2021 were integrated into the final result for every city. Two of the total 24 overpasses fall within the northern hemispheric summer months (both in June).

2.1.1 OCO-2/3 XCO_2

The column-averaged dry-air mole fraction of CO_2 (XCO_2) is retrieved from the reflected sunlight over two CO_2 bands centered on 1.6 and 2.0 μm and the oxygen-A band for obtaining surface pressure (Eldering et al., 2019; Taylor et al., 2020). In addition to the standard Nadir, Glint, and Target modes, OCO-3 collects several adjacent swaths of XCO_2 observations over a spatial area of approximately 80 km by 80 km during its SAM mode, e.g., four individual swaths in an overpass over LA on Feb 24, 2020 (**Fig. 2a**). Similar to OCO-2, each satellite swath is comprised of eight spatial footprints/soundings and each sounding has an area of ∼1.6×2.2 km^2 at nadir (**Fig. 2a**). Our analysis only used screened OCO-3 B10r/B10p4r data (Eldering, 2021) with an XCO_2 quality flag of zero (QF = 0). It is worth highlighting the B10r/B10p4r product is superior to the Early version of OCO-3 (Taylor et al., 2020) including improved geo-location, advanced radiometric calibration, improved quality filters, and customized post processing bias correction. As OCO-3 is mounted on the International Space Station that is in a precessing orbit, its overpass time varies, for example, from 07:00 to 15:00 local time for the overpasses we examined, unlike OCO-2.

2.1.2 TROPOMI XCO

The TROPOMI column density of CO molecules [mole cm^{-2}] is retrieved via the measured radiation from shortwave infrared wavebands centered at ∼2.3 μm (Veefkind et al., 2012). We selected soundings with quality assurance $\geq$ 0.5 as recommended by the TROPOMI README document (Landgraf et al., 2020) and converted the column density to the total column-averaged dry-air mole fraction of CO [XCO in ppb] by calculating the dry-air column density [mole cm^{-2}] from retrieved surface pressure and total column water vapor. TROPOMI CO is retrieved at a larger pixel area of ∼7×7 km^2 at Nadir and reduced to 5.5×7 km^2 after Oct 6, 2019 (**Fig. 2c**). The overpass time of TROPOMI is ∼13:30 local time of equatorial overpass for nadir measurements with a time span of 1–2 hours for soundings on the edge of its wide swath (i.e., ∼2600 km).

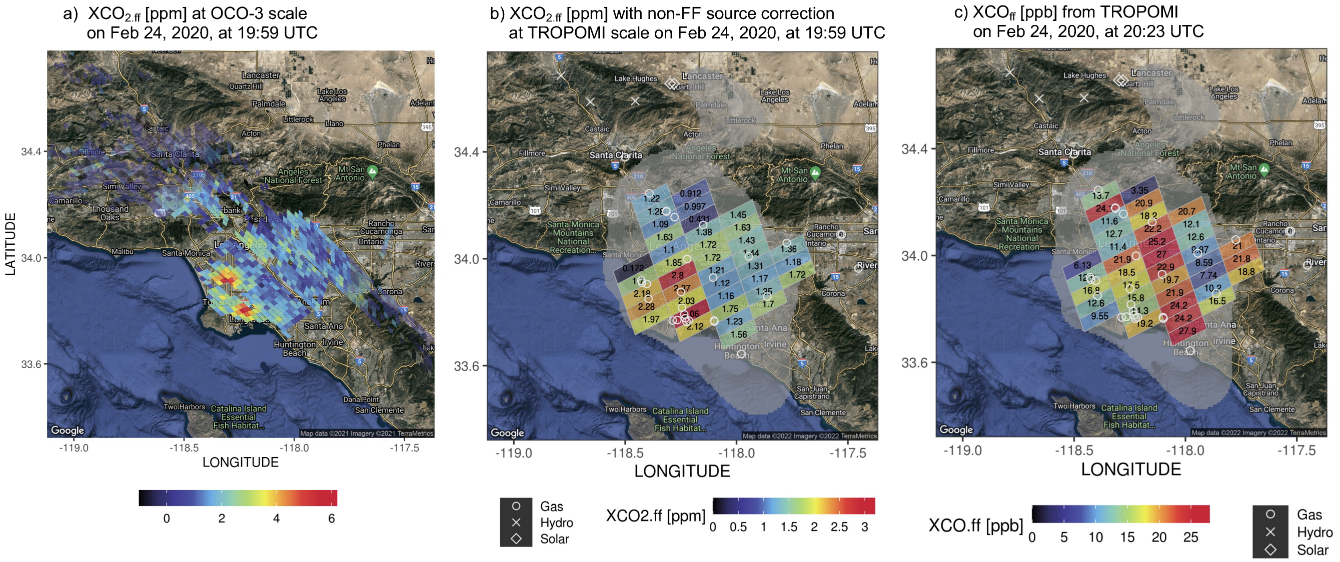

Figure 2. Spatial maps of FF XCO_2 enhancements with corrections of non-FF sources at native OCO-3 scale (a, ppm) and aggregated at the TROPOMI scale (b, ppm) along with FF XCO enhancements (c, ppb) over Los Angeles on Feb 24, 2020. Power stations with different primary fuel types are displayed in different white symbols based on the Global Power Plant Dataset (World Resources Institute, 2018). The overall X-STILT column footprint [ppm / (μmol m^{-2} s^{-1})] from all soundings is drawn in light grey (see explanations for column footprint in **Sect. 2.2.1**). The underlying hybrid maps were created using the ggmap library in R with the hybrid view of Google Maps over LA (copyright: Map data ©2021 Imagery ©2021 TerraMetrics).

2.1.3 Differences between two sensors/species

Four mismatches between OCO-3 XCO_2 and TROPOMI XCO pose challenges in extracting FF enhancements and ER_{CO} from atmospheric observations, which are accounted for in this analysis:

1. *Satellite pixel area:* XCO_2 enhancements from multiple OCO-2/3 soundings falling within a given TROPOMI polygon are grouped and averaged (**Fig. 2a vs. b**). For simplicity, the centered lat/lon coordinate of an OCO pixel is used to determine its corresponding TROPOMI polygon. The retrieval uncertainty tied to each OCO sounding is also aggregated according to the TROPOMI sampling, contributing to the total observational uncertainty (**Sect. 2.2.4**).

2. *Averaging kernel profile:* Within the planetary boundary layer where most emissions occur, TROPOMI XCO retrieval is affected by cloud height/fractions, which yields lower-than-unity AK (**Supplementary Fig. S1**). OCO-2/3 XCO_2 under cloudy conditions are typically omitted from Lite files and when QF = 0 is applied; thus, its AK normally approaches one near the surface for cloud-free scenes. The mismatch in AKs between sensors must be accounted for as it can affect the interpretation of ERs. In this work, we accounted for AKs within an atmospheric transport model (**Sect. 2.2.1**).

3. *Overpass times, meteorological conditions, and emission variations:* As a result of the overpass time difference between sensors, variations in meteorological conditions (e.g., wind direction and speed) can lead to changes in urban plume shapes detected by the two sensors as they pass by. We dealt with changes in wind speed and wind direction separately. The former is resolved by the "scaling factor" inferred from an atmospheric transport model and the latter undergoes manual evaluations (**Sect. 3.1**). Besides, CO and CO_2 emissions themselves can vary over the course of a day, e.g., driven by road transportation and residential sectors. Given the overpass time difference between sensors, it is likely that such mismatch in the timing of CO versus CO_2 emissions may affect the observed ER_{CO}.

4. *Non-fossil fuel sources/sinks:* The lack of account of influence from the biosphere and biomass burning may bias ER_{CO}. Given our definition of a local background, the contrast in non-FF concentration anomalies between the urban and the background region needs to be included (for more explanation, see **Sect. 2.2.3**).

2.2 Estimates of E_{gas}, ER_{CO} and uncertainties

Previous studies (Mitchell et al., 2018; Wu et al., 2020; Lin et al., 2021) proposed an approach to calculate an overall CO_2 or CH_4 flux using atmospheric measurements and atmospheric transport model, without relying on prior information from emission inventories. Here we briefly describe this approach to obtain the overall emission of either CO_2 (**Eq. 1**) or CO (**Eq. 2**) for a single sounding S, modified from Wu et al. (2020):

$$\langle E_{\mathrm{CO_2,s}} \rangle = \frac{\mathrm{X_{ffCO_2,s}}}{\langle \mathrm{XF_{CO_2,s}} \rangle} = \frac{\mathrm{X_{obsCO_2,s}} - \mathrm{X_{bgCO_2}} - \delta \mathrm{X_{bioCO_2,s}} - \delta \mathrm{X_{bbCO_2,s}}}{\iint \mathrm{XF_{CO_2,s}(x,y)\,dx\,dy}}. \tag{1}$$

$$\langle E_{\mathrm{CO,s}} \rangle = \frac{\mathrm{X_{ffCO,s}}}{\langle \mathrm{XF_{CO,s}} \rangle} = \frac{\mathrm{X_{obsCO,s}} - \mathrm{X_{bgCO}} - \delta \mathrm{X_{bbCO,s}}}{\iint \mathrm{XF_{CO,s}(x,y)\,dx\,dy}}. \tag{2}$$

All the X terms in the numerator contribute to the estimate of FF column enhancements (X_{ff}, **Fig. 2**). X_{ff} at a downwind satellite sounding S is the net result of FF sources over the source region (x, y). To describe the source region and attribute it to each satellite sounding, we adopted the column version of the Stochastic Time-Inverted Lagrangian Transport (X-STILT) model (Lin et al., 2003; Fasoli et al., 2018; Wu et al., 2018). From this model, we obtain a "scaling factor" $\langle XF_{\text{gas}} \rangle$ to account for the sounding-specific AK profile and meteorology (**Sect. 2.2.1**). X_{bg} denotes the local background values using satellite observations uncontaminated by the city emission, which are constant for a group of background observations. The background region is usually chosen over rural region outside the urban plume with consideration of wind direction (**Sect. 2.2.2**). From a Lagrangian viewpoint, the air parcels arriving at an urban sounding might be traced back to different origins from the air parcels arriving at a rural sounding, meaning observations at the two soundings may be influenced differently by the surrounding biosphere. Hence, two background correction δ-terms are attached to account for the urban-background gradient in concentration anomalies due to net ecosystem exchange (NEE) and biomass burning (**Sect. 2.2.3**).

For a given sounding, the estimated flux $\langle E_{\text{gas}} \rangle$ with unit of μmol m^{-2} s^{-1}represents the average emission over the corresponding source region of that sounding, which should not be confused with the direct emission at that sounding location. The ER_{CO} for a given sounding S is then derived from **Eqs. 1 & 2** as follows:

$$ER_{\text{CO,s}} = \frac{\langle \text{E}_{\text{CO,s}} \rangle}{\langle \text{E}_{\text{CO}_{2,\text{s}}}\rangle} = \frac{\text{X}_{\text{ffCO,s}}}{\text{X}_{\text{ffCO}_{2,\text{s}}}} \frac{\langle \text{XF}_{\text{CO}_{2,\text{s}}}\rangle}{\langle \text{XF}_{\text{CO,s}}\rangle} = \frac{\text{X}_{\text{ffCO,s}}}{\text{X}_{\text{ffCO}_{2,\text{s}}}} \gamma_{\text{foot,s}}, \tag{3}$$

where $\frac{X_{\text{ffCO,s}}}{X_{\text{ffCO}_{2,\text{s}}}}$ is the observed enhancement ratio and $\gamma_{\text{foot,s}}$ measures how enhancement ratios without considering AKs and meteorology differ from emission ratios. We simply use ppb-CO/ppm-CO_2 for units of ER_{CO} (same as mmol-CO/mol-CO_2).

2.2.1 The X-STILT model

The X-STILT model is adopted in this study, 1) to provide the scaling factor $\langle XF_{\text{gas}} \rangle$ that resolves differences in AKs and changes in wind speeds; 2) to identify an overpass-specific urban plume for determining background regions (**Sect. 2.2.2**); and 3) to estimate the sounding-specific biogenic and pyrogenic anomalies for background corrections (**Sect. 2.2.3**).

STILT releases an ensemble of air parcels from target observations (known as the "receptor") and tracks the movement of those air parcels backward in time. The source region corresponding to each sounding is informed by the "source-receptor relation" or the STILT "footprint" (Lin et al., 2003; Fasoli et al., 2018). The STILT footprint [ppm / (μmol m^{-2} s^{-1})] describes the change in atmospheric concentration [ppm] at a downwind location due to possible upwind sources/sinks [μmol m^{-2} s^{-1}]. The magnitude of STILT footprints tends to be higher close to the target observation or under steadier wind conditions, thus, air parcels within the boundary layer can interact more closely with fluxes from the surface.

To accommodate the use of satellite-based column data, X-STILT incorporates retrieval-specific AK and pressure weighting profiles to the footprint calculation (Wu et al., 2018), such that the influence on air parcels originating from various altitudes of an atmospheric column are weighted by the sounding- and sensor- specific vertical profile (**Supplementary Fig. S2**). The "column footprint" (XF_{gas}) measures the sensitivity of the total column concentration to upwind fluxes from the perspective of a specific satellite sensor. For instance, XF_{gas} for TROPOMI XCO differs from XF_{gas} for OCO-2/3 XCO_2 even for concurrent observations. Since the air flow arriving at each satellite observation is unique, the magnitude and spatial distribution of $\mathrm{XF_{gas}}$ vary across soundings (**Supplementary Fig. S3**). By taking an average of these sounding-dependent column footprints, as shown in **Supplementary Fig. S3**, we can identify the source region for all soundings in a SAM (light gray area in **Fig. 2b,c**). In this work, we only traced air parcels back for 12 hours to calculate column footprints, which is sufficient to capture the near-field influence from the target city and better aligned with the local background region outside the city (**Sect. 2.2.2**).

In short, the spatial summation of column footprints $\langle XF_{\mathrm{gas}} \rangle$ is regarded as a scaling factor to address the sounding-specific meteorological condition and AK profile. The term γ_{foot} as derived from **Eq. 3** reveals the difference between a simple enhancement ratio and a more robust, model-corrected emission ratio.

2.2.2 Background definition X_{bg}

Defining accurate background levels to extract urban FF enhancements has always been a challenge in top-down analysis, especially when dealing with column measurements with small signal-to-noise ratio. Wu et al. (2018) compared several approaches to determine a localized $\mathrm{XCO_2}$ background for extracting urban signals from OCO-2, including approaches that 1) solely use satellite observations with statistics (e.g., daily median); 2) solely use an atmospheric transport model (e.g., the "curtain method" based on global concentration fields); and 3) combine observations and transport information from models. Here, we expand the third approach to arrive at localized swath-dependent background values. The broader spatial coverage and multiple swaths stretching out of the city domain of OCO-3 SAMs help improve such background determination by introducing spatial variations in the background, compared to the narrow swath of OCO-2. Accurately describing latitudinal or spatial gradients in background $\mathrm{XCO_2}$ has been emphasized recently (Ye et al., 2020; Schuh et al., 2021).

The process of background determination used in this work involves a first step of identifying the urban plume and differentiating soundings as within or outside of the plume. To outline the urban plume shape at the overpass time, we utilized the forward mode of STILT with the inclusion of wind uncertainty into atmospheric dispersion. Specifically, 1000 air parcels were released continuously from a rectangle representing the city domain (dashed black box in **Fig. 3**) every 30 minutes starting from 10 hours ahead of the overpass time. All air parcels are allowed to travel forward in time for 12 hours from their initial release times. A random wind component typifying model-data wind errors is added to the parcel dispersion (Lin and Gerbig, 2005). We subset the air parcels only during the overpass time and applied a 2-dimensional kernel density estimate (KDE) based on parcels' spatial distributions (blue to purple contours in **Fig. 3**). KDE is carried out using the kde2d function provided by the MASS library in R (Venables and Ripley, 2002). These normalized KDE contours indicate the likelihood and shape of an urban plume when the satellite scans through. The extent of the urban plume is finalized using a normalized KDE contour of 0.15 (black curve in **Fig. 3**), which is proper to 1) include soundings with possible influence from the target city and 2) exclude observations elevated by another city (e.g., red polygons centered at ~32°N and 120°E in **Fig. 3c**). This procedure is carried out separately for OCO-2/3 and TROPOMI to reveal the impact of changing meteorology on urban plumes at different overpass times (see **Sect. 3.1**). It is worth stressing that only enhancements within the urban plume are used for $\mathrm{ER_{CO}}$ estimates.

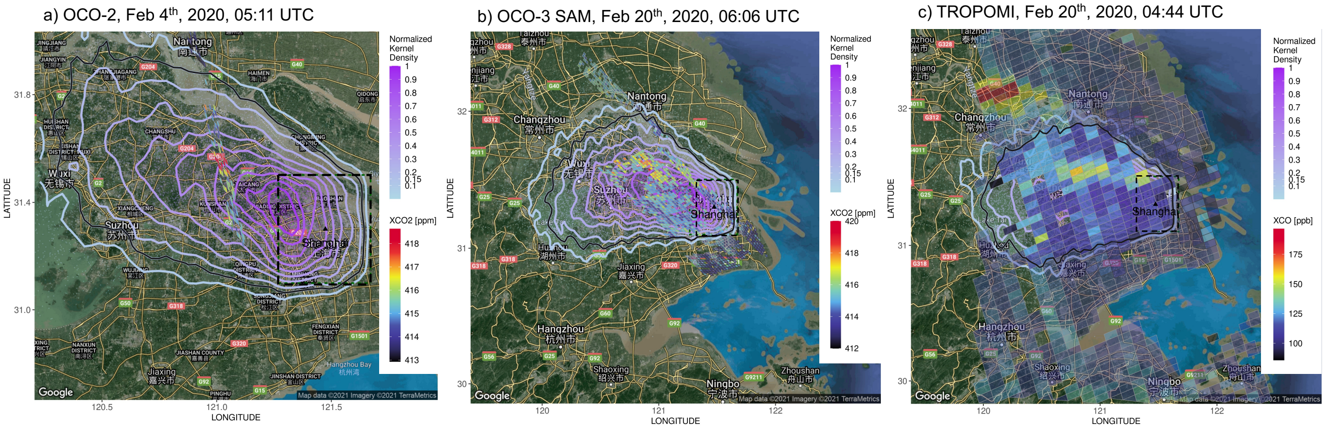

Figure 3. Demonstrations of background determination from OCO-2 XCO_2 on Feb 4, 2020 (a), OCO-3 SAM XCO_2 [ppm] and TROPOMI XCO [ppb] on Feb 20, 2020 (b, c) over Shanghai. The model-based urban plume (solid black curve) is determined by the normalized 2-D kernel density of the air parcels' distribution during the overpass time (blue-purple contours). The "background soundings" outside the urban plume are highlighted with black outlines, while other soundings are outlined in white. For example, OCO-2 observations to the north outside the plume (∼121.1°E, 31.9°N, a) and OCO-3 and TROPOMI soundings to the southeast outside the plume (b, c) are used to estimate background values and background uncertainties. The underlying hybrid maps were created using the ggmap library in R with the hybrid view of Google Maps over Shanghai (copyright: Map data ©2021 Imagery ©2021 TerraMetrics).

Next, the background value is calculated as the median value of observed X_{gas} per swath over the background region. For example, the background region is the area to the east outside the urban plume since southeasterly wind dominates (**Fig. 3b,c**). Background values vary with swaths if an OCO-3 SAM is examined. We chose the median instead of the mean to minimize the impact of any "outliers" that may be from a second FF source (other than our target cities) in the background region. Background uncertainty is estimated as a component of the total observed uncertainty (**Sect. 2.2.4**).

2.2.3 Background correction terms for non-FF sources/sinks

The swath-dependent local background approach described above explicitly assumes equal contributions from non-FF sources and sinks for soundings in the background versus soundings in the urban plume, which may not always be the case. We then correct for the spatial gradient in contributions from biogenic and pyrogenic fluxes.

As proposed in Wu et al. (2021), rather than absolute biogenic concentration anomalies, it is the contrast in these anomalies between the background versus the urban plume that is required, considering our localized background definition. Specifically, hourly X-STILT column footprints are convolved respectively with hourly mean NEE from a biospheric model representation and daily mean wildfire emissions from the Global Fire Assimilation System (GFAS, Kaiser et al., 2012) to estimate the sounding-specific absolute column anomalies X_{bio} and X_{bb}. The Solar-Induced Fluorescence (SIF) for Modeling Urban biogenic Fluxes (SMUrF, Wu et al., 2021) model estimates gross primary production (GPP) from a Contiguous SIF product (CSIF trained based on OCO-2 SIF, Zhang et al., 2018) and respiration based on modeled SIF-based GPP, air and soil temperatures.

Next, the urban-background gradient in such anomalies is calculated as the difference between sounding-specific anomalies and the mean anomaly within the background region:

$$\delta X_{\mathrm{bioCO_2}}(\mathrm{s}) = \mathrm{X}_{\mathrm{bioCO_2}}(\mathrm{s}) - \overline{\mathrm{X}_{\mathrm{bioCO_2}}(\mathrm{s_{bg}})} \tag{4}$$

where s or $\mathrm{s_{bg}}$ represents all the soundings or select soundings in the background region, respectively. Let us imagine a summer day at noon in the north hemisphere, the urban core is normally associated with a weaker biospheric uptake than the surrounding rural region. Biogenic signals $X_{\mathrm{bioCO_2}}(\mathrm{s})$ for soundings in the city are less negative than the mean biogenic signal over the rural background $\overline{X_{\mathrm{bioCO_2}}(\mathrm{s_{bg}})}$. Hence, the urban-background biogenic gradient $\delta X_{\mathrm{bioCO_2}}(\mathrm{s})$ is normally positive and be subtracted from the total column (**Eq. 1**). Estimated X_{bio} and their urban-background gradient δX_{bio} are shown in **Sect. 3.1**.

Flux exchanges from the ocean and chemical transformation (e.g., CO sink via hydroxyl radical (OH) and source from oxidation of volatile organic compounds, VOCs) are not considered. The average lifetime of CO against OH ranges from a few weeks to several months depending on the season, much longer than the few-hour timescale we care about. Yet, CO can be generated from the oxidation of $\mathrm{CH_4}$ and non-methane VOCs at various rates, which is discussed in **Sect. 4.3**.

2.2.4 Uncertainty sources

The uncertainty related to emissions should contain uncertainties from 1) the atmospheric transport (i.e., column footprints), 2) observations, and 3) non-FF sources and sinks, according to **Eqs. 1 or 2**. We neglect uncertainties from column footprints assuming no transport bias exists during either OCO or TROPOMI overpass time. The urban-background gradient in non-FF fluxes remains very small compared to FF enhancements (**Sect. 3.1**).

We estimated uncertainties of observed FF enhancements following **Eq. 5**. As previously described, observations from a few screened OCO soundings ($\sim$ 5 to 28 OCO soundings depending on the TROPOMI footprint size) are averaged to arrive at mean $\mathrm{XCO_2}$ at the TROPOMI scale. Due to such averaging/binning process, the $\mathrm{XCO_2}$ uncertainty due to binning is considered using the standard deviation of $\mathrm{XCO_2}$ observations ($\sigma^2_{\varepsilon,bin}$ in **Eq. 5**) within a TROPOMI polygon.

$$\sigma^2_{\varepsilon,obs} = \sigma^2_{\varepsilon,bin} + \sigma^2_{\varepsilon,bg} + \sigma^2_{\varepsilon,retrv}. \tag{5}$$

$\sigma^2_{\varepsilon,bin}$ is not required for estimating XCO uncertainty. Background uncertainty ($\sigma^2_{\varepsilon,bg}$) contains both the retrieval error and the variability of column observations (as standard deviation) within background regions.

The retrieval uncertainty ($\sigma^2_{\varepsilon,retrv}$) of XCO is available for each TROPOMI sounding, whereas that of $\mathrm{XCO_2}$ is reported for individual OCO-2/3 sounding (as read from Level 2 Lite files), which need to be aggregated at the TROPOMI scale. Due to possible correlations in retrieval errors between nearby OCO soundings, we estimated the error correlation length scale (L_x) using exponential variograms as demonstrated in **Supplementary Fig. S4**. Within a TROPOMI polygon that contains N numbers of OCO soundings, an error variance-covariance matrix with a dimension of $N \times N$ is constructed with its diagonal elements filled with OCO sounding-specific retrieval error variance. Then, L_x is used to form the normalized covariance matrix, i.e., $exp(-\frac{D(S_i,S_j)}{L_x})$ where $D(S_i,S_j)$ denotes the distance between each two OCO soundings ($1 \leq i < j \leq N$). Lastly, the sum of all elements in the error covariance matrix (both variance and covariance elements) is divided by N^2 to obtain one $\sigma^2_{\varepsilon,retrv}$ per TROPOMI grid. As a result, the overall uncertainty of FF enhancement per sounding is often predominated by the background error component.

2.3 Identifying ER$_{\mathrm{CO}}$ for heavy industry within a city

A key objective of this study is to explain the intra-city variability of ER$_{\mathrm{CO}}$ by exploring sector-specific or sector-dominant combustion activities. While certain combustion processes and sectors tend to have higher ERs than others, the sectoral-dependent ER are likely variable within and across cities. The ERs derived from atmospheric observations comprise a mixed effect of different activities in the city. Previous attempts include reducing the number of sectors and relying on prior sector-specific ERs via a (joint) Bayesian inversion (Brioude et al., 2012; Nathan et al., 2018).

Here, we propose a novel approach to identify ERs associated with the heavy industry in a city. Instead of relying on prior emission inventories that can sometimes be erroneous regarding the magnitude and the location of sector-specific activities (see discussions in **Sect. 4.4**), we utilized an urban land cover classification dataset, WUDAPT that provides Local Climate Zone (LCZ) classifications at a grid spacing of 120 m (Ching et al., 2018). As shown in **Fig. 4a, d**, LCZ categories include street canyons (e.g., compact/open/lightweight, high-/mid-/low-rise), building spacing (e.g., sparsely built, heavy industry), and tree spacing (e.g., dense/scattered trees, low plants, rocks, etc). Each LCZ is unique in its thermal, radiative, and metabolic properties. For instance, compact high-rise (LCZ 1) and heavy industry (LCZ 10) categories have the highest anthropogenic heat output of 50–300 W m^{-2} and > 300 W m^{-2}, respectively (Stewart and Oke, 2012). Heavy industry is defined as low-rise and mid-rise industrial structures (towers, tanks, stacks) and mostly paved or hard-packed metal with steel and concrete construction materials with few or no trees in WUDAPT (Ching et al., 2018), which differs from the industry-relevant sectors defined by the Intergovernmental Panel on Climate Change (e.g., as used in EDGAR). We clarify that we are not trying to tackle individual industrial processes, which is much more difficult. LCZ maps are only available for a limited number of cities including Shanghai and LA as of this analysis but have recently been generalized to the entire globe (Demuzere et al., 2022).

To relate ER$_{\mathrm{CO}}$ to heavy industry, the percentage of heavy industry is first interpolated at 1 km grid spacing from WUDAPT LZC maps (%, **Fig. 4c, f**). The industrial coverage map is then convolved with the X-STILT column footprint (**Supplementary Fig. S3**) to quantify the industrial influence on each TROPOMI polygon $P_{ind}(x, y)$, which is defined as the column footprint-normalized industry fraction (**Supplementary Fig. S5**). For example, soundings in the city center farther away from the heavy industry in LA are related to smaller influences. Lastly, we sum $P_{ind}(x, y)$ across the space to arrive at $\langle P_{ind} \rangle$, serving as a metric of how much the observation at a given sounding is affected by heavy industry. Specifically, soundings with $\langle P_{ind} \rangle$ larger than the 75^{th} or 90^{th} percentiles are marked as locations "impacted" or "strongly impacted" by heavy industry within the city. Sensitivity and significance analyses are conducted and presented in **Sect. 3.2.2** to test if: 1) the results are subject to the percentile threshold when defining industry-dominated soundings, and; 2) ERs over industry-dominated soundings are statistically significantly different from ERs for the remaining soundings.

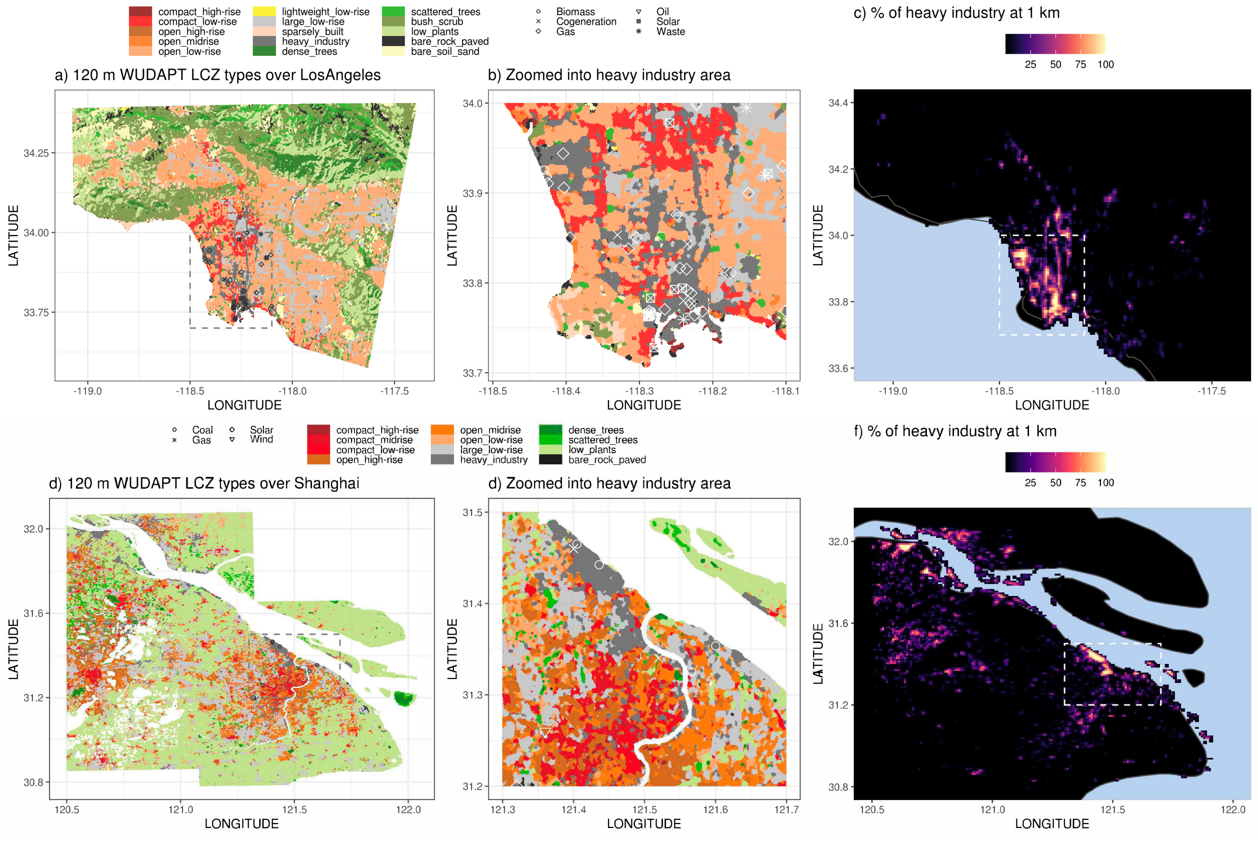

Figure 4. Maps of 120 m Local Climate Zone (LCZ) from WUDAPT (a and d) with magnified images (b and e) and an interpolated areal coverage of heavy industry [%] at 1 km around Shanghai and Los Angeles (c, f). LCZ classifications centered on Wuxi and Shanghai are combined. Power stations based on the Global Power Plant Dataset (WRI, 2018) are drawn as white symbols. The dashed light gray or white rectangles in the maps indicate the magnified region.

3 Results

$\mathrm{ER_{CO}}$ values and uncertainties are reported at multiple spatial scales from the spatially-resolved sounding level (**Eq. 3**) to the overall overpass- and city- level. Again, only ERs at soundings within the urban plume are selected. Overpasses with too few valid soundings in a plume area are also removed from the results. Before presenting ERs at different spatial scales, we assess factors that may influence the derived $\mathrm{ER_{CO}}$.

3.1 Interference factors that modify $\mathrm{ER_{CO}}$

We examine impacts on $\mathrm{ER_{CO}}$ from the following interference factors: 1) differences in AKs between OCO-2/3 $\mathrm{XCO_2}$ and TROPOMI XCO; 2) shifts in wind fields between two overpass times; 3) urban-background contrast in biogenic and pyrogenic contributions; and, 4) temporal variation in emission themselves. In summary, we found that difference in AKs and wind directions between sensors can significantly affect the spatially-resolved $\mathrm{ER_{CO}}$. For the final 24 overpasses we selected, temporal variations in the emission pattern and urban-background gradients in biogenic/pyrogenic contributions play minor roles in overpass- or city-level ERs.

Recall that sounding-specific AKs and wind speeds were being considered in the sounding-specific column footprint using X-STILT (**Sect. 2.2**) and the $\gamma_{\mathrm{foot}} = \frac{\langle XF_{\mathrm{CO_2}} \rangle}{\langle XF_{\mathrm{CO}} \rangle}$ suggested their combined impacts on spatially-resolved $\mathrm{ER_{CO}}$ (**Supplementary Fig. S6c**). For instance, mean γ_{foot} spans from 1.20 to 1.57 over LA and from 1.02 to 1.38 over Shanghai across different overpasses (printed in **Fig. 7a, c**). γ_{foot} is generally larger than 1 because AKs near the surface of TROPOMI XCO are smaller than surface AKs for OCO-2/3. Simply using enhancement ratios without accounting for mismatches in AKs and wind speeds between sensors will likely lead to an underestimation of emission ratios (**Eq. 3**). On average, overpass-level $\mathrm{ER_{CO}}$ can be $\sim$20% higher than enhancement ratios across our 24 overpasses.

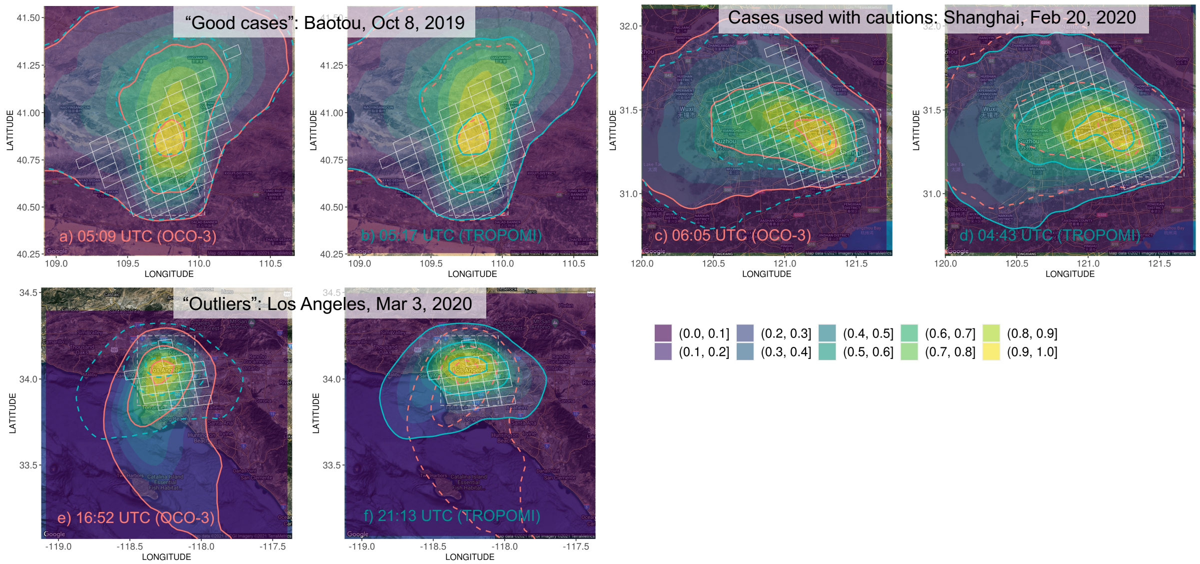

Figure 5. Examples of modeled urban plumes during OCO-3 (red curve) and TROPOMI (blue curve) overpass times in UTC. The likelihood of these meteorology-only urban plumes (no emission involved) is quantified by the normalized KDE binned by 10 intervals of the modeled air parcel distribution (yellow-green-purple contours). Three types of overpasses are shown as follows: 1) "good cases" with almost identical urban plumes at two times, e.g., Baotou on Oct 8, 2019 with Δt of 8 mins (a, b); 2) cases to be used with caution where the urban plume shifts from one time to another and requires a simple plume rotation, e.g., Shanghai on Feb 20, 2020 with Δt of 1.5 hours (c, d); 3) outliers where two urban plumes change significantly, e.g., for Los Angeles on March 3rd, 2020 with Δt of over 4 hours (e, f). The underlying hybrid maps were created using the ggmap library in R with the hybrid view of Google Maps over LA (copyright: Map data ©2021 Imagery ©2021 TerraMetrics).

The second factor is the change in wind directions between two overpass times, which is evaluated using the same algorithm as the urban plume detection in **Sect. 2.2.2**. Again, colored contours and curves in **Fig. 5** indicate neither the intensity of concentrations nor flux fields (as no prior emissions are used), but rather the likelihood of urban plumes determined by atmospheric dispersion with random wind uncertainties. Matching between OCO-3 soundings and TROPOMI polygons as described earlier would be fine for concurrent observations (**Fig. 5a, b**); but becomes problematic if Δt becomes large ("outliers" with significant changes in plumes in **Fig. 5e, f**). The cases between "good cases" and "outliers" are to be used with caution (**Fig. 5c, d**).

By comparing the overlap of plumes at the two times, we shifted OCO-3 soundings to better align with TROPOMI polygons. For example, on Feb 20, 2020, because the modeled plume at the OCO-3 overpass time (06:06 UTC) appears northward compared to the plume at the TROPOMI overpass time (04:44 UTC), OCO-3 soundings were shifted southward by 0 to 2 grids depending on their longitudinal coordinates (**Supplementary Fig. S7**). In other words, by shifting FF XCO_2 enhancements, we better align the urban plume at OCO-3 time with the plume at TROPOMI time. Every OCO-TROPOMI coincidence has been manually examined and assigned to one of the three categories, which are further summarized in **Sect. 4.1**. “Outliers” are removed from this analysis, since no simple wind or plume rotation would improve their ER_{CO} estimates.

Besides changes in wind directions, CO and CO_2 emissions themselves can vary across daytime hours, likely driven by the road transportation and residential sectors. As a result, variations in the derived ER_{CO} across multiple overpasses may reflect not only the variation in combustion efficiencies but also the mismatch in the emission timing. LA may be one of the cities with more distinct daytime changes in emissions compared to industry-centered cities. Fortunately, based on a supplementary sensitivity analysis using measurements from the Total Carbon Column Observing Network in Pasadena (TCCON, Wennberg et al., 2017), by limiting satellite overpasses to those with a smaller time difference, ER_{CO} appear to be less variable (**Supplementary Fig. S8**). Future geostationary satellite monitoring NO_x (e.g., TEMPO, Chance et al., 2022) may provide better guidance towards the hourly pattern in urban emissions, especially from the traffic sector with more daytime fluctuations, which have been discovered using surface monitoring networks (e.g., over Chicago; de Foy, 2018).

The last factor is the urban-background contrast in contributions from non-FF sources and sinks. The modeled biogenic XCO_2 anomaly using SMUrF and X-STILT ranges from -0.7 to 0.3 ppm per OCO-3 sounding, depending on the hour of a day (i.e., solar zenith angle), season and wind direction (**Supplementary Fig. S9**). As explained in **Sect. 2.2.2**, urban-background gradients in these biogenic anomalies (i.e., δX_{bio}) were used to correct the constant localized background X_{bg} (**Eq. 1**). Take the two overpasses with the largest urban-background contrast as examples: as biospheric uptake is normally weaker in urban areas than surrounding rural areas (often as background regions), the urban-rural gradient for locations in the plume region becomes more positive (**Supplementary Fig. S10b**). Nonetheless, even for the one summertime SAM over Zibo on June 21, 2020, sounding-level δX_{bio} ranges from 0 to 0.4 ppm, which remains small compared to sounding-level $FFCO_2$ enhancements of 2 to 7 ppm (**Supplementary Fig. S11a, b**). For most other overpasses, δX_{bio} aggregated to TROPOMI sampling stay low with an absolute value < 0.3 ppm (as printed in each panel of **Figs. 6 & 7**). Even with a bias in the resultant δX_{bio} resulting from incorrect prior NEE, the effect on derived FF enhancements and ER_{CO} would be small.

Although LA is surrounded by occasional intense wildfire activities, column anomalies due to biomass burning suggested by the coupling of GFAS and X-STILT are minimal for the dates we examined. Yet, since wildfire-related ER_{CO} are usually higher than FF-related ER_{CO} (**Fig. 1**), the proper account of pyrogenic contributions and gradients between urban and surrounding rural areas is important for cities in mountainous and forested areas during fire seasons. For instance, Crounse et al. (2009) leveraged aircraft measurements of HCN and C_2H_2 over Mexico City as indicators to disentangle CO signals due to biomass burning and urban emissions, respectively.

3.2 Intra-city ER_{CO} variations and signals from heavy industry

Observed enhancements are the net consequence of associated sources/sinks from source regions. That is, high atmospheric content of CO_2 or CO at the sounding location does not necessarily indicate a high emission rate at this location (Kiel et al., 2021). Our derived emissions and ERs, although reported for each sounding, indicate the overall emission and combustion efficiency over its source region.

In the following subsections, we present ERs for each sounding and the aggregate for each overpass and city. Since aggregating sounding-level ERs to a single value per overpass or city is sensitive to the adopted method/statistic, we bootstrapped E_{CO} and E_{CO_2} based on their sounding-specific values and uncertainties to generate a linear regression fit per bootstrap loop (light grey lines in **Fig. 6**). Specifically, 1,000 random sets of E_{CO} and E_{CO_2} were generated following assumed normal distributions, where sounding-level emission estimates provide mean statistics with observational uncertainties as standard deviations. We used the standardized major axis (SMA) solution for linear regression to minimize deviations of data points from the regression line for both axes. Eventually, we obtained 1,000 bootstrapped slopes and selected slopes with positive values, which yield the overpass-level ER_{CO} and uncertainty (e.g., colored dashed lines and text in **Fig. 6**). Besides, sounding-level ER_{CO} from all overpasses are presented in histograms and generally follow a log-normal distribution (**Fig. 7b, d**).

City	Total power capacity (MW) and by fuel types	Key industry OR annual crude steel capacity (kt yr^{-1})
Los Angeles	5,808 MW (95.6% fueled by gas; 0% by coal)	refinery, shipping
Shanghai	16,031 MW (75.2% fueled by coal; 24.4% by gas)	iron & steel (25,099 kt yr^{-1})
Baotou	6,470 MW (100% fueled by coal)	iron & steel (12,619 kt yr^{-1})
Zibo (w/ Zouping)	9,720 MW (100% fueled by coal)	electrolytic aluminum; iron & steel (2,532 kt yr^{-1})

Table 1. A summary of total power generation capacity (Global Power Plant Dateset by World Resources Institute, 2018) and information on heavy industry including annual crude iron capacity (GID, Wang et al., 2019). Power plants are selected from a $0.5° \times 0.5$ °region around each city with percentage generated by the main fuel types.

3.2.1 Baotou and Zibo

Combustion efficiencies are generally poor for these two industry- and energy- oriented cities. The overpass-specific ERs span from 9.3±1.2 to 24.6±3.8 mmol $mol^{-1}$with an integrated city-level estimate of 17.3±0.5 mmol $mol^{-1}$for Baotou (**Fig. 6a**). According to GID, the Baotou iron and steel group is located within the city and contributes to an annual capacity of crude iron of 12,619 kt yr^{-1} with estimated CO_2 emissions of 20,462 kt yr^{-1} (**Table 1**). The slightly lower ER_{CO} and FF enhancements in Feb 2021 coincides with the timing of the Spring Festival in 2021 (∼Feb 12). SDs of bootstrapped slopes are higher for overpasses with fewer high-quality satellite soundings, e.g., 3.8 mmol $mol^{-1}$for overpasses with seven available TROPOMI polygons in the urban plume on May 31, 2020. Utilizing the bootstrap method helps account for the impact of sounding numbers on the overall city-level ER estimate.

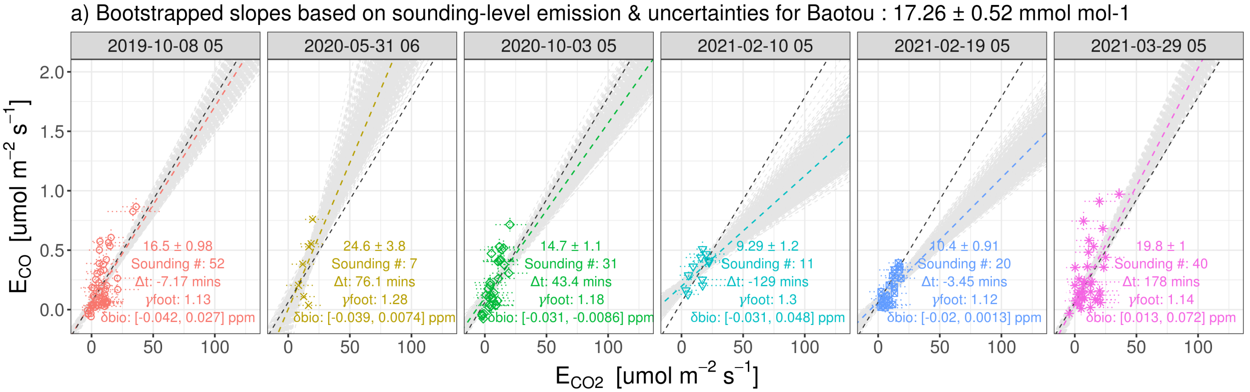

a) Bootstrapped slopes based on sounding-level emission & uncertainties for Baotou : 17.26 ± 0.52 mmol mol-1

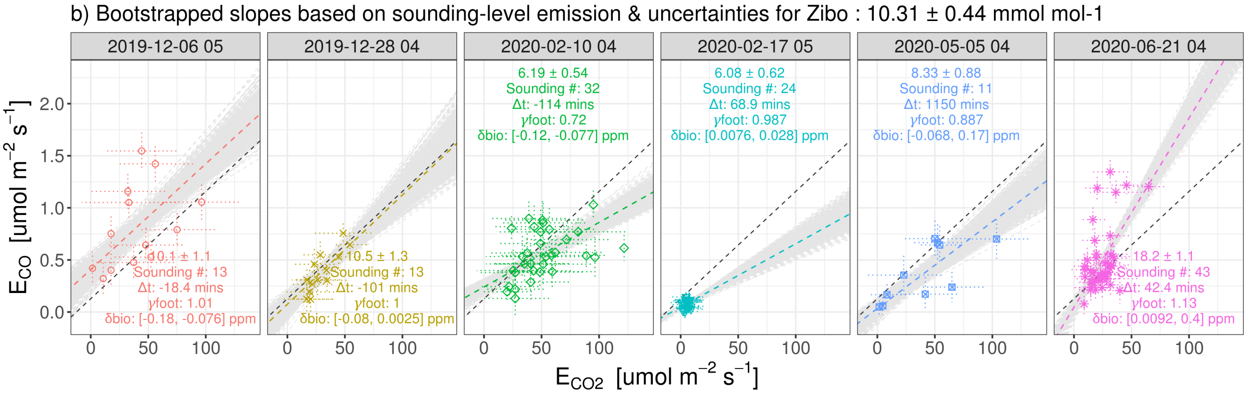

b) Bootstrapped slopes based on sounding-level emission & uncertainties for Zibo : 10.31 ± 0.44 mmol mol-1

Figure 6. Scatter plots of CO and CO_2 fluxes [μmol m^{-2} s^{-1}] and their uncertainties (error bars in dotted lines) for Baotou (a) and Zibo (b). Linear regressions are applied for the data from each overpass (dashed colored lines) and all overpasses (dashed black line). Only bootstrapped regression lines with positive slopes were chosen from the Monte Carlo experiment (dashed gray lines; $\sim$ 98.4% and 93.3% of the total 6,000 bootstrapped lines for Baotou and Zibo, respectively). TROPOMI overpass time in UTC, total TROPOMI sounding numbers, discrepancies in overpass times (Δt, mins), impacts from AK and wind conditions between sensors ($\gamma_{\rm foot}$), and the range of urban-rural biogenic gradient ($\delta X_{\rm bio}$, ppm) are labelled in each panel. XCO_2 on Dec 6 and Dec 28, 2019 over Zibo are the Nadir OCO-3 observations.

Zibo with the nearby county-level city Zouping accounts for over 1/8 of the total coal consumption of Shandong province in 2017. The coal-fired power plants in the area contribute to a total power generation capacity of 9,720 MW (**Table 1**), which are likely to support local metal industries especially the production of electrolytic aluminum (world's top producers). The maximum XCO_2 enhancement per OCO-3 sounding can even reach up to 10 ppm for a few overpasses (not shown). Interestingly, ER_{CO} for Zibo first declined from 10.1±1.1 mmol mol^{-1}to 6.1±0.6 mmol mol^{-1}during Feb 2020 and gradually increased back to 18.2±1.1 mmol mol^{-1}by June 2020 (**Fig. 6b**). Such temporal variations in ER_{CO} agree nicely with the timing of the initial phase of COVID-19 lockdown in China (i.e., Feb to May in 2020) (e.g., Laughner et al., 2021). We suspect changes in ER_{CO} could be driven by the partial shut-down and re-opening of the multiple coal-fired power plants and metal industries in the area.

3.2.2 Los Angeles and Shanghai

Although OCO-3 has sampled the Los Angeles basin dozens of times to date, many overpasses did not pass the quality check (i.e., QF) and were removed from the final result due to their noticeable shifts in urban plumes between two overpass times (e.g., March 3, April 15, and May 5, 2020 for LA; discussed in **Sect. 4.1**). The overpass-level ER ranges from 7.4±0.8 to 11.7±1.5 mmol-CO/mol-CO_2 with a city-level value of either 9.6±0.5 mmol mol^{-1}informed using the regression approach (**Fig. 7a**) or 9.7 mmol mol^{-1}using the histogram approach (**Fig. 7b**). Our space-based ER_{CO} estimates over LA fall within the reported range of 7.1 to 12.4 mmol $mol^{-1}$from prior studies (Wennberg et al., 2012; Brioude et al., 2013; Hedelius et al., 2016; Silva and Arellano, 2017). Small discrepancies in ER_{CO} between studies may be attributed to discrepancies in the time of interest, sampling strategies, and techniques for ER_{CO} calculations (e.g., background definition).

In contrast to LA, where urban plumes are usually well-constrained with the basin, wind speeds and directions vary across different overpasses over Shanghai —i.e., southeasterly wind on Feb 4 and Feb 20, 2020; southwesterly wind on Feb 24, 2020 and Feb 19, 2021; and northerly wind on April 23 and Dec 30, 2020. Such changes in the wind regimes between overpasses over Shanghai suggest that soundings from an individual overpass may reflect emission patterns over different source regions, which emphasizes the importance of integrating atmospheric transport in interpreting temporal variations in observation-based ERs. In other words, one cannot simply use all the soundings over a city to calculate ERs, but need to select those soundings that are actually affected by emissions from that city. The overpass-specific ER ranges from 4.2±1.2 to 17.1±6.2 mmol $mol^{-1}$with a city-level average of 10.2±0.4 mmol mol^{-1}based on the linear regression approach (**Fig. 7c**) or 12.9 mmol mol^{-1}using the histogram approach (**Fig. 7d**).

Now we focused on the distribution of sounding-level ERs for these two megacities (**Fig. 7b, d**) to see if ERs associated with a part of the city (i.e., heavy industry region) can be revealed. As described earlier, to locate the soundings affected or strongly affected by heavy industry in a city with the account of overpass-specific meteorology, we coupled the LZC-based industrial coverage (**Fig. 4c, f**) with X-STILT column footprints and quantified the industrial influence, $\langle P_{ind} \rangle$, at each sounding location.

Industrial regions within the LA basin are concentrated to the south near the Port of LA and to the west of downtown near Los Angeles Airport and the Chevron Refinery in El Segundo (**Fig. 4e**). The distribution of ERs for industry-dominated soundings tends to shift slightly towards the lower end (blue or red bars in **Fig. 7b**) compared to the distribution for all soundings (gray bars in **Fig. 7b**). For example, ERs > 15 ppb $ppm^{-1}$are less frequently found for industry-dominated soundings (red bars in **Fig. 7b**). The industry-oriented soundings generally have slightly lower CO but higher CO_2 enhancements (**Fig. 2b, c**), compared to other soundings within the basin, resulting in slightly lower ER_{CO}. No iron and steel facilities or coal-fired power plants are found over the heavy industry area in LA according to GID and GEM. We hypothesize that the slight shift of ER_{CO} towards the lower end may be explained by heavy-duty diesel engines and natural gas power plants occupying the Port of LA versus predominately gasoline vehicles across the city, because ER_{CO} for heavy-duty diesel vehicles and non-coal-fired power plants are generally lower than that for light-duty gasoline vehicles. For example, by splitting observations for daytime versus nighttime, a field campaign in 2007 in Beijing suggested that the ER linked to nighttime diesel transportation is much lower than the gasoline sub-sector (Westerdahl et al., 2009, **Fig. 1a**). Similar to LA, higher fuel efficiency was found over the ship channel of Houston (ER of ∼4 ppb ppm^{-1}) compared to downtown Houston (ER of ∼10 ppb ppm^{-1}) (Brioude et al., 2012, **Fig. 1b**). Unfortunately, only two good SAMs are available near Houston from late 2019 to June 2021, but future work can further validate the urban-industry contrast in ERs from space.

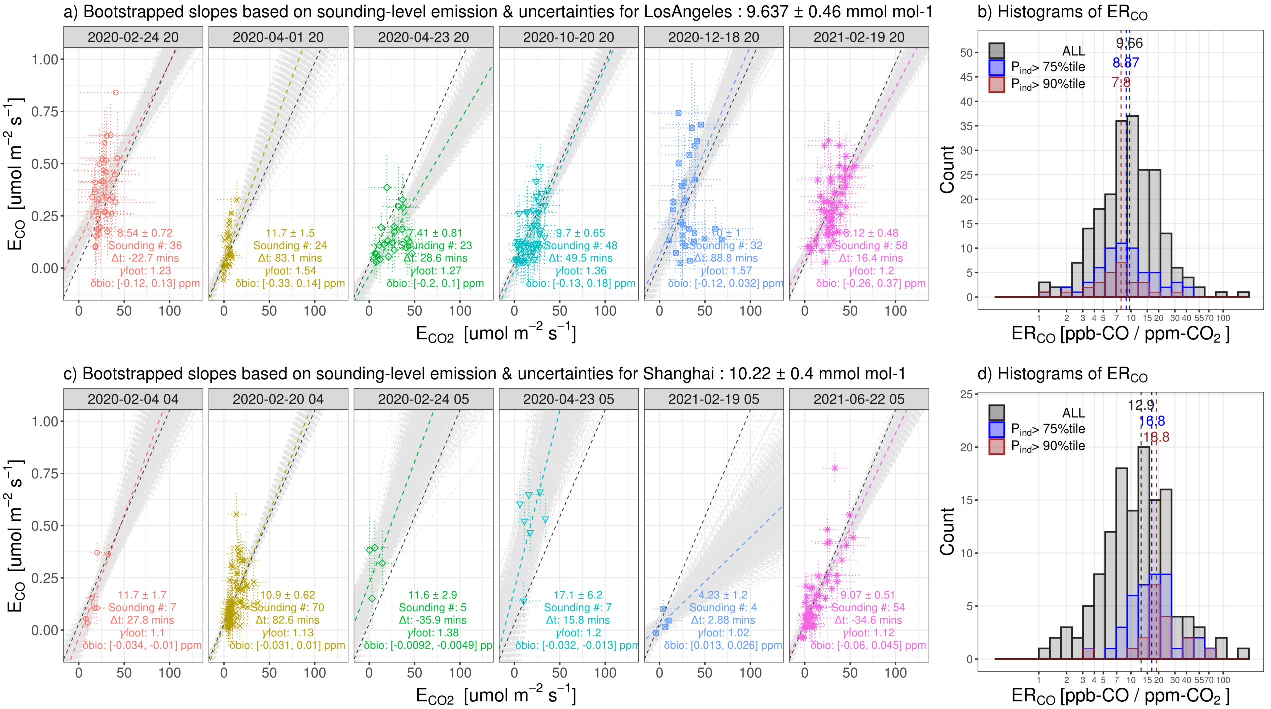

Figure 7. a, c) Same as **Fig. 6** but for LA and Shanghai. Only bootstrapped regression lines with positive slopes are presented as light grey lines (∼ 94.3% and 88.4% of the 1000 bootstrapped lines per overpass for LA and Shanghai, respectively). b, d) Histogram of $\mathrm{ER_{CO}}$ for all soundings (black bars); soundings impacted or strongly impacted by heavy industry are defined using $\langle P_{ind} \rangle$ larger than their 75^{th} or 90^{th} percentiles (blue or red bars) with corresponding median ERs (vertical dashed lines). The industrial impact is quantified using column footprints from X-STILT (to inform atmospheric transport) together with localized information from the urban land cover data WUDAPT.

For Shanghai, the heavy industry is concentrated to the north of the city center (**Fig. 4a**). Interestingly, in contrast to LA, ERs affected by heavy industry are skewed towards the higher end with medians of 16.8 or 18.8 ppb ppm^{-1}(blue or red bars in **Fig. 7d**), compared against the city-level median of 12.9 ppb ppm^{-1}(black bars in **Fig. 7d**). CO and $\mathrm{CO_2}$ enhancements and $\mathrm{ER_{CO}}$ are all higher for industry-oriented soundings than those for all soundings combined. Such spatial divergence in enhancements and ERs between heavy industry and the entire city may be attributed to substantial CO emissions from iron and steel production. Schneising et al. (2019) also found that many hotspots with high TROPOMI CO enhancements in China and India are tied to iron and steel industries. During such production processes, iron ores are reduced to crude iron and steel where CO is involved. According to the plant level estimate in 2019 from GID, Baoshan Iron & Steel Co., Ltd. located to the north of downtown Shanghai has an annual crude steel capacity of 25,099 kt yr^{-1} (**Table 1**) and a total $\mathrm{CO_2}$ emission of 32,148 kt yr^{-1} for all coke, sinter, iron, and crude steel combined.

To validate the robustness in such ER shifts related to heavy industry, we tested different percentile thresholds other than 75^{th} and 95^{th} used to determine industry-dominated soundings (**Sect. 2.3**). The above statements on industry-impacted $\mathrm{ER_{CO}}$ hold if using alternative thresholds including the 50^{th}, 60^{th}, 80^{th} percentiles. Additional Welch two-sample t-test confirms that ERs from industry-dominated soundings significantly differ from the remaining soundings less affected by heavy industry. When the adopted percentile threshold increases from 50^{th} to 95^{th}, divergence in ERs between industrial vs. non-industrial soundings becomes more apparent and the p-value for statistical significance in such difference becomes smaller (with p-values < 0.05 for all thresholds). In addition, the average number of OCO-3 soundings in a TROPOMI polygon is roughly the same for industry-affected soundings versus the rest (e.g., 11.8 vs. 10.3 for LA and 7.3 vs. 8.7 for Shanghai).

We acknowledged that although many iron/steel plants may aim at combusting as much CO as possible before releasing CO into the atmosphere, the indispensable role CO played in the iron/steel industry makes it unique when assessing its $\mathrm{ER_{CO}}$ and combustion efficiency among various industrial processes. Furthermore, it is difficult to separate combustion signals of individual sectors from observations without prior assumptions on sector-specific contributions, since atmospheric concentration at a given location is comprised of various underlying combustion processes spread over the source region. Even using additional co-emitted species, it would be risky to assume that a co-emitted species (e.g., CO or $\mathrm{NO_x}$) solely comes from one individual emission sector.

4 Discussion

This study is one of the first to analyze intra-city variations of emission ratios between CO and $\mathrm{CO_2}$ using two asynchronous satellite sensors. We describe 1) complications induced by discrepancies between satellite sensors and retrievals and 2) demonstrate methods to mitigate these complications by accounting for sounding-specific averaging kernels, atmospheric transport, and urban-background contrast in the contribution from non-FF sources/sinks using an atmospheric transport model.

4.1 Influence from non-FF components and atmospheric transport

Pyrogenic anomalies are minimal for the overpasses we examined, but should be considered for certain cities (e.g. during dry seasons over Mexico City, Crounse et al., 2009) considering the high $\mathrm{ER_{CO}}$ from forest wildfires of 35 to 80 ppb $\mathrm{ppm^{-1}}$(**Fig. 1a**). Most overpasses we analyzed fall within the dormant seasons. For the three overpasses during the growing season, modeled biogenic anomalies using the SMUrF model for a given OCO-2/3 sounding may reach up to 0.5 ppm (**Supplementary Fig. S9**). Even though modeled NEE and resultant biogenic contributions/gradient can be uncertain, we stress again it is the urban-background biogenic contrast (δX_{bio} in **Eq. 1**) that is important for estimating $\mathrm{FFCO_2}$ enhancements given our setup for a local background value. Satellite missions such as TROPOMI and the upcoming Geostationary Carbon Cycle Observatory (GeoCarb) will provide Solar-Induced Fluorescence (SIF), which may help improve spatially-explicit SIF-based GPP and NEE estimates (Turner et al., 2020; Wu et al., 2021), specifically by reducing the dependence on other remote sensing products and the assumption of model parameters for each plant functional type.

The biggest challenge affecting the robust estimate of spatially-resolved $\mathrm{ER_{CO}}$ is the shift in wind directions between two overpass times. Substantial changes in wind directions and urban plumes (e.g., "outliers" in **Fig. 5e, f**) were mostly found for overpasses with an absolute time difference $|\Delta t|$ of >2 hours (implied by the bars attached with an asterisk in **Fig. 8**). If TROPOMI pixel sizes are relatively large (i.e., non-nadir observations) or the wind is steadier, this $|\Delta t|$ constraint may be relaxed, as long as emissions for a specific city is less driven by sectors with noticeable diurnal cycle (e.g., road transportation). For instance, on May 31, 2020, TROPOMI polygon sizes for the industry-dominated city Baotou are sufficiently large compared to the shift in urban plumes despite its $|\Delta t|$ of 3 hours (**Fig. 8**). In addition, we manually re-positioned the OCO-3 soundings to TROPOMI polygons for a few cases (bars with non-zero numbers on top in **Fig. 8**) using a simple wind/plume shift demonstrated in **Sect. 3.1**. Fortunately, future geostationary satellites will be capable of mapping XCO and $\mathrm{XCO_2}$ simultaneously at a higher temporal frequency, which will eliminate this issue.

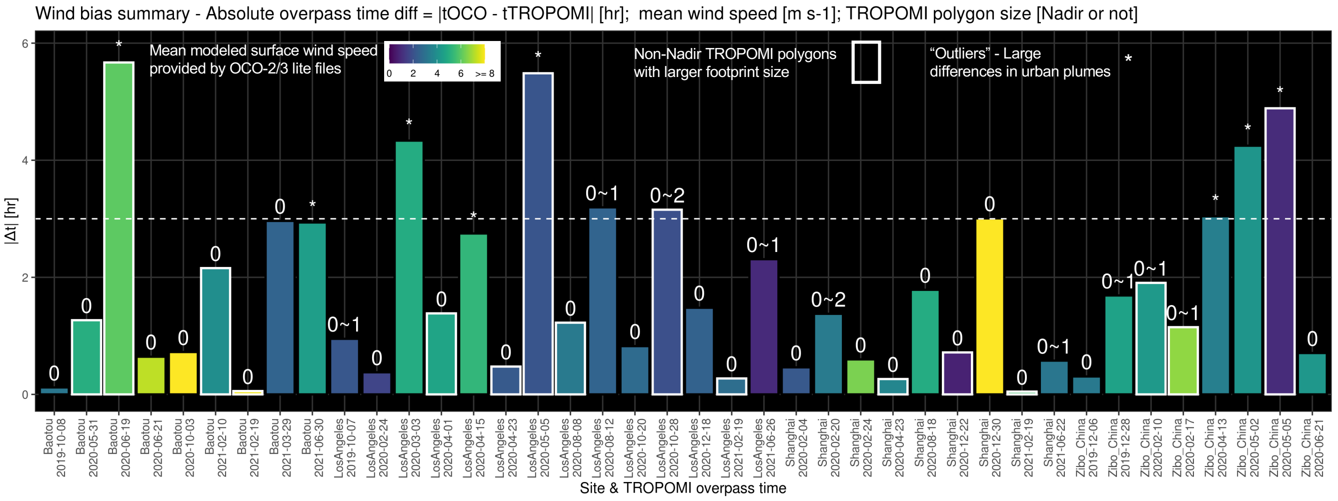

Figure 8. A summary of wind directional shift between OCO-2/3 versus TROPOMI overpass times. The y-axis denotes the absolute time difference ($|\Delta t|$ in hours) per overpass. The color of the bar represent the instantaneous modeled surface wind speed [m $\mathrm{s^{-1}}$] from OCO-2/3 Lite files. Bars labelled with an asterisk indicate that urban plumes between two overpass times differ so much that they cannot be brought into agreement with a simple plume rotation. The number on each bar (e.g., 0∼1) denotes the number of TROPOMI polygons needed to be shifted to align the urban plumes at two times. For example, 0∼1 means that TROPOMI polygons over certain locations are shifted by one grid. Bars labelled with zero on top do not require a manual plume shift. Bars with white outline indicate that the sampled TROPOMI soundings on that date are non-nadir with larger pixel size.

4.2 ERs for individual sounding, overpass, city, and heavy industry region within a city

Contrary to previous work relying on inventory-based sector-based ERs, we attribute the intra-urban gradient to heavy industry using an urban land cover classification dataset. Such high-resolution localized maps help identify the observations strongly influenced by heavy industry. Based on a limited sample size, the heavy industry within the greater Shanghai area is tied to an $\mathrm{ER_{CO}}$ higher than the city average reflecting a relatively poorer combustion efficiency (**Fig. 7d**). Industry- and energy-centered cities like Baotou and Zibo are less efficient in their combustion activities. In particular, industry-dominated ERs over

Shanghai (18.8 mmol mol^{-1}as indicated by the dashed red line in **Fig. 7d**) align better with the overall city-scale ER over Baotou of 17.3 mmol mol^{-1}(**Fig. 6**). The previously reported urban-integrated ER_{CO} values are mostly constrained within the range of 5 to 20 ppb ppm^{-1}with a few exceptions over 30 ppb ppm^{-1}in east Asia before 2010 (**Fig. 1**). Our city-level estimates from space agree well with the range of previously reported values.

Reporting one city-scale ER_{CO} from spatially-explicit ERs can be subject to 1) the adopted statistic, 2) overpass dates and overpass-specific wind conditions, and 3) estimated uncertainties in ER_{CO}. For example, overall ER derived from all soundings within the urban plume differs from ER derived from a selection of soundings. Even though we started with all quantified OCO-2/3 observations in a SAM, only those located within the urban plumes (black curve in **Fig. 3**) can be used to estimate ERs, which is an unbiased way to compare ERs from overpasses with different meteorological conditions. The mean or median value of sounding-level ER_{CO} (e.g., 13.4 or 9.6 ppb ppm^{-1}for LA in **Supplementary Fig. S12**) differs slightly from the city-average using the regression slope method when observational uncertainties were taken into account (e.g., 9.6 ppb ppm^{-1}for LA in **Fig. 7a**). Apart from these bulk quantities, the distribution of ER_{CO} in the linear space are negatively-skewed and roughly follow the log-normal distribution (**Supplementary Fig. S12**), where a few observations with higher ER_{CO} are influenced by point sources with poorer combustion efficiency. More observations with finer satellite pixels across the city would improve the robustness in both the spatial distribution and bulk estimates of ERs.

4.3 Limitation

The main limitation of this work is the relatively low sample size largely constrained by the requirement for small differences in overpass times. When more satellite data or upcoming data from geostationary satellites become accessible, intra-city ERs can be used to more robustly assess the temporal variation in sector-oriented combustion efficiency, including across seasons or times (e.g., business-as-usual scenarios versus pandemic-disturbed time frames). Beyond the sheer number of soundings, uncertainty arises when aggregating CO_2 enhancements from the finer resolution OCO-3 grid to the TROPOMI sampling. The centered lat/lon coordinates of OCO-2/3 soundings are chosen to decide the corresponding TROPOMI polygon, while a very few OCO soundings may be located right on the boundary of TROPOMI polygons. Nevertheless, we find no significant bias associated with the number of OCO soundings per TROPOMI polygon regarding the heavy industry analysis.

Another factor that we did not explicitly account for is the secondary CO production from both anthropogenic and biogenic VOCs (AVOCs, BVOCs). Under a cascade of reactions in favorable conditions, VOCs emitted from the upwind source location are oxidized to CO at various rates, which result in possible higher CO at the downwind sounding location and a divergence between enhancement ratios and emission ratios. As BVOCs are usually associated with shorter lifetimes compared to many AVOCs (e.g., Surl et al., 2018), we discuss BVOCs and AVOCs separately. BVOCs can contribute significantly to the total CO source at the regional scale especially during growing seasons (e.g., Miller et al., 2008; Hudman et al., 2008; Gonzalez et al., 2021). However, since BVOCs like biogenic CO_2 come mainly from rural areas outside the city, by subtracting localized CO background using CO observations outside the urban plume, the impact from BVOCs on the derivation of CO enhancements would be minimized. The lifetime of most AVOCs remains long enough, except for a few species including alkenes (Surl et al., 2018). Without a good observational constraint of the VOC composition and group-specific emissions for different cities around the globe over the years, it would be challenging to accurately quantify the impact on atmospheric XCO and ER_{CO} due to AVOCs emitted from urban areas or specifically from industrial areas. More future efforts regarding urban VOCs may include 1) exploring what good proxies can be measured from space that well represent the bulk AVOC characteristics (e.g., formaldehyde, Zhu et al., 2014) and 2) interpreting such observations, e.g., by utilizing chemical transport models for source attribution (Gonzalez et al., 2021). Note that the noise/uncertainty in current daily TROPOMI formaldehyde observations may be too large for daily resolved analyses.

4.4 Implications for inventory evaluation

This work provides insights towards estimating emission ratios from future satellite sensors, as ERs help pinpoint hotspots with poor combustion efficiency, which to inform sub-city emission/pollution control efforts.

Satellite-based ER estimates help evaluate sector-specific emission factors and source locations adopted in bottom-up emission inventories (e.g., Silva and Arellano, 2017). Substantial contrast in both the magnitude and spatial distribution of enhancement ratios can be found between the observations and forward simulations (using X-STILT column footprints and sectoral emissions from EDGARv5). Take Shanghai as an example, simulated enhancement ratios using prior emissions appear to be much higher (> 50 ppb ppm^{-1}, **Supplementary Fig. S13b**) than observed ratios (mostly < 30 ppb ppm^{-1}, **Supplementary Fig. S13a**). Regarding the spatial distribution, simulated enhancement ratios using total FF emissions mimic simulated enhancement ratios using only industry-related emissions (**Supplementary Fig. S13b versus c**); and both simulated ratios differ substantially from observed enhancement ratios. Such model-data mismatch may result from inaccurate activity data and emission factors of EDGAR as well as atmospheric transport uncertainties. This preliminary analysis illustrates that satellite observations of trace gases could be used to evaluate emission factors adopted in bottom up emission inventories. More sophisticated approaches such as flux inversions (Hedelius et al., 2018; Brioude et al., 2011, 2012; Palmer et al., 2006) may better constrain sector-specific CO and CO_2 emissions from inventories.

Spatial proxies including nightlight data from the Black Marble (https://blackmarble.gsfc.nasa.gov/) and urban land cover data can support not only the development of emission inventories but also sector-orientated evaluations with atmospheric observations of CO_2 and co-emitted pollutants. This work demonstrates the benefit of using high-resolution urban land cover classifications to provide independent information about locations of various anthropogenic activities, building structures, and vegetation coverage.

5 Conclusion

We investigated fossil fuel combustion efficiency by quantifying the emission ratio of CO and CO_2 across Los Angeles, Shanghai, Baotou, and Zibo (Zouping), using nearly coincident observations of TROPOMI XCO and OCO-2/3 XCO_2. Multiple swaths of observations collected by OCO-3 SAMs cover a much broader area relative to OCO-2 swaths, facilitating the determination of background values and the separation of emission signals from different parts of a city. We incorporate spatial gradients in background values by calculating the background per swath and correcting for the urban-background gradient due to non-anthropogenic sources and sinks. Sensor-specific averaging kernel profiles and meteorological conditions were accounted for using an atmospheric transport model (X-STILT). The ratio between XCO and XCO_2 enhancements without considering such sensor-specific factors is normally lower than the emission ratio. Cases with severe asynchronicity, specifically overpass time differences over 3 hours, correspond to significant changes in urban plumes. Properly accounting for the overpass-specific meteorological condition or source-receptor relationship and identifying only the soundings influenced by urban emissions is critical for estimating ER for cities, which is realized using an atmospheric transport model. Such model approach is then used to identify soundings strongly affected by heavy industry. As a result, the overall city-level ER_{CO} for Shanghai (10.2±0.4 mmol mol^{-1}) is slightly larger than that for Los Angeles (9.6±0.5 mmol mol^{-1}). Industry-related ER_{CO} for Shanghai are much larger than its city-level average; whereas industry-related ER_{CO} for LA are slightly lower than its city-level average. ERs tied to heavy industry regions in Shanghai (18.8 mmol mol^{-1}) are approximately equal to the city-level ER_{CO} for the industry-orientated city of Baotou (17.3±0.5 mmol mol^{-1}). High ERs highlight the poor combustion efficiency tied to certain industrial activities, e.g., metal productions (**Table 1**).

With future satellites (e.g., GeoCarb, TEMPO, CO2M) providing better spatial and temporal coverage of XCO_2 and relevant co-located tracer observations, it will be possible to monitor and verify temporal trend and variation in the combustion efficiency over hotspots within an urban area, which will provide significant guidance for urban planning and emission control.

Code and data availability. OCO-3 L2 B10r XCO_2 data and TROPOMI XCO data were accessed from https://doi.org/10.22002/D1.2046 and 10.5270/S5P-1hkp7rp, respectively. X-STILT code has been modified to work with TROPOMI data archived on github branch at https://github.com/uataq/X-STILT. We kindly ask the users to follow the code policy in utilizing and acknowledging the X-STILT code for interpreting TROPOMI column data. Hourly NEE fluxes from SMUrF are archived on Oak Ridge National Lab DAAC at https://doi.org/10.3334/ORNLDAAC/1899.

Appendix A: List of prior studies collected in Figure 1

Sector in **Fig. 1a**	Location	Years	Reference	Additional notes
Traffic	Denver, US	1997	Bradley et al. (2000)	
Traffic	Switzerland	2004	Vollmer et al. (2007), Table 2	Gubrist Tunnel
Traffic	CONUS	2005-2007	Bishop and Stedman (2008)	Chicago, Denver, Los Angeles, Phoenix
Traffic	Paris	2012	Ammoura et al. (2014), Table 2	Tunnel (congestion vs. moving)
Traffic	Switzerland	2011	Popa et al. (2014), Table 1	Islisberg Tunnel (moving)
Traffic	Beijing, China	2007	Westerdahl et al. (2009)	diesel heavy-duty vs. gasoline light-duty
Shipping	China	2011	Zhang et al. (2016), Table 3	Diesel engines; Estimated from EFs
Shipping	Western Europe	2007	Moldanová et al. (2009), Table 5	Diesel engine; Estimated from EFs
Shipping	Texas	2006	Williams et al. (2009), Figure 2	Diesel engines; Estimated from EFs
Biomass burning	Global	NA	Akagi et al. (2011), Table 1-2	Estimated from EFs

Urban areas in **Fig. 1b**	Observation years	Reference
Los Angeles (LA)	2002 and 2010	Brioude et al. (2013)
LA	2007-2008	Djuricin et al. (2010)
LA	2008 and 2010	Wennberg et al. (2012)
LA	2010	Silva et al. (2013); Silva and Arellano (2017)
LA	2013-2016	Hedelius et al. (2016)
LA	2019-2021	**This study**, Figure 7
Pasadena	2007	Wennberg et al. (2012), Table 2
Sacramento	2009	Turnbull et al. (2011a), Sect. 3.2
Indianapolis (Indy)	2012-2014	Turnbull et al. (2015)
Salt Lake City (SLC)	2015-2016	Bares et al. (2018), Table 2
Edinburgh	2005	Famulari et al. (2010), Table 1
Paris	2010	Lopez et al. (2013)
Paris	2010-2014	Ammoura et al. (2016), Table 1
London	2006	Harrison et al. (2012), Figure 27
London	2012	O'Shea et al. (2014), Table 3
London	2016	Pitt et al. (2019), Table 2
Rotterdam	2011	Super et al. (2017)
Germany Alps	2012-2013	Ghasemifard et al. (2019)
Hungary	2017	Haszpra et al. (2019), Table 1
St. Petersburg	2019	Makarova et al. (2021)
Miyun	2004-2008	Wang et al. (2010), Table 2
Beijing	2006	Han et al. (2009), Figure 11
Shangdianzi	2009-2010	Turnbull et al. (2011b)
Nanjing	2011	Huang et al. (2015), Sect. 3.4.2
Seoul	2016	Tang et al. (2018), Table 3
Seoul	2019	Sim et al. (2020), Table 2
Jingdezhen	2017-2018	Xia et al. (2020), Table 3
Zibo, Baotou, Shanghai	2019-2021	**This study**, Figures 6-7

Author contributions. DW designed and carried out this analysis. JL, POW, and PIP supervised this study. RRN, MK, and AE provided the bias-corrected B10 data for OCO-3 SAMs used in this work. All authors participated in the interpretation of the results and paper writing plus editing.

595 *Competing interests.* The authors declare no conflict of interests.

Acknowledgements. The production of the OCO-3 science data products used in this paper was carried out at the Jet Propulsion Laboratory, California Institute of Technology, under a contract with the National Aeronautics and Space Administration [prime contract number 80NM0018D0004]. The research effort was funded by the Jet Propulsion Laboratory Research and Technology Development project R.21.023.106. The analysis is supported by the W.M. Keck Institute for Space Studies and by the National Aeronautics and Space Administration (grant number 80NSSC21k1064). The computations presented here were conducted in the Resnick High Performance Computing Center, a facility supported by Resnick Sustainability Institute at the California Institute of Technology. The first author appreciates the discussion with Joshua Laughner, Eric Kort, Tomohiro Oda, and John Lin. We thank Julia Marshall and the second anonymous referee for their careful read of our submitted manuscript and for their constructive suggestions that have helped improve our study.

References

Akagi, S., Yokelson, R. J., Wiedinmyer, C., Alvarado, M., Reid, J., Karl, T., Crounse, J., and Wennberg, P.: Emission factors for open and domestic biomass burning for use in atmospheric models, Atmospheric Chemistry and Physics, 11, 4039–4072, 2011.

Ammoura, L., Xueref-Remy, I., Gros, V., Baudic, A., Bonsang, B., Petit, J. E., Perrussel, O., Bonnaire, N., Sciare, J., and Chevallier, F.: Atmospheric measurements of ratios between CO_2 and co-emitted species from traffic: A tunnel study in the Paris megacity, Atmospheric Chemistry and Physics, 14, 12 871–12 882, https://doi.org/10.5194/acp-14-12871-2014, 2014.

Ammoura, L., Xueref-Remy, I., Vogel, F., Gros, V., Baudic, A., Bonsang, B., Delmotte, M., Té, Y., and Chevallier, F.: Exploiting stagnant conditions to derive robust emission ratio estimates for CO_2 , CO and volatile organic compounds in Paris, Atmospheric Chemistry and Physics, 16, 15 653–15 664, https://doi.org/10.5194/acp-16-15653-2016, 2016.

Bares, R., Lin, J. C., Hoch, S. W., Baasandorj, M., Mendoza, D. L., Fasoli, B., Mitchell, L., and Stephens, B. B.: The wintertime covariation of CO_2 and criteria pollutants in an urban valley of the Western United States, Journal of Geophysical Research: Atmospheres, 123, 2684–2703, 2018.

Bishop, G. A. and Stedman, D. H.: A decade of on-road emissions measurements, Environmental Science & Technology, 42, 1651–1656, 2008.

Bradley, K. S., Brooks, K. B., Hubbard, L. K., Popp, P. J., and Stedman, D. H.: Motor vehicle fleet emissions by OP-FTIR, Environmental Science and Technology, 34, 897–899, https://doi.org/10.1021/es9909226, 2000.

Brioude, J., Kim, S. W., Angevine, W. M., Frost, G. J., Lee, S. H., McKeen, S. A., Trainer, M., Fehsenfeld, F. C., Holloway, J. S., Ryerson, T. B., Williams, E. J., Petron, G., and Fast, J. D.: Top-down estimate of anthropogenic emission inventories and their interannual variability in Houston using a mesoscale inverse modeling technique, Journal of Geophysical Research Atmospheres, 116, https://doi.org/10.1029/2011JD016215, 2011.

Brioude, J., Petron, G., Frost, G. J., Ahmadov, R., Angevine, W. M., Hsie, E. Y., Kim, S. W., Lee, S. H., McKeen, S. A., Trainer, M., Fehsenfeld, F. C., Holloway, J. S., Peischl, J., Ryerson, T. B., and Gurney, K. R.: A new inversion method to calculate emission inventories without a prior at mesoscale: Application to the anthropogenic CO_2 emission from Houston, Texas, Journal of Geophysical Research Atmospheres, 117, https://doi.org/10.1029/2011JD016918, 2012.

Brioude, J., Angevine, W. M., Ahmadov, R., Kim, S. W., Evan, S., McKeen, S. A., Hsie, E. Y., Frost, G. J., Neuman, J. A., Pollack, I. B., Peischl, J., Ryerson, T. B., Holloway, J., Brown, S. S., Nowak, J. B., Roberts, J. M., Wofsy, S. C., Santoni, G. W., Oda, T., and Trainer, M.: Top-down estimate of surface flux in the Los Angeles Basin using a mesoscale inverse modeling technique: Assessing anthropogenic emissions of CO, NOx and CO_2 and their impacts, Atmospheric Chemistry and Physics, 13, 3661–3677, https://doi.org/10.5194/acp-13-3661-2013, 2013.

Chance, K., Liu, X., Suleiman, R., Abad, G. G., Zoogman, P., Wang, H., Nowlan, C., Huang, G., Sun, K., Al-Saadi, J., et al.: TEMPO Green Paper: Chemistry experiments with the Tropospheric Emissions: Monitoring of Pollution instrument, 2022.

Chandra, N., Lal, S., Venkataramani, S., Patra, P. K., and Sheel, V.: Temporal variations of atmospheric CO_2 and CO at Ahmedabad in western India, Atmospheric Chemistry and Physics, 16, 6153–6173, https://doi.org/10.5194/acp-16-6153-2016, 2016.

Ching, J., Mills, G., Bechtel, B., See, L., Feddema, J., Wang, X., Ren, C., Brousse, O., Martilli, A., Neophytou, M., et al.: WUDAPT: An urban weather, climate, and environmental modeling infrastructure for the anthropocene, Bulletin of the American Meteorological Society, 99, 1907–1924, 2018.

Crisp, D., Fisher, B., O'Dell, C., Frankenberg, C., Basilio, R., Bösch, H., Brown, L., Castano, R., Connor, B., Deutscher, N., et al.: The ACOS CO 2 retrieval algorithm–Part II: Global X CO 2 data characterization, Atmospheric Measurement Techniques, 5, 687–707, 2012.

Crounse, J., DeCarlo, P., Blake, D. R., Emmons, L., Campos, T., Apel, E., Clarke, A., Weinheimer, A., McCabe, D., Yokelson, R. J., et al.: Biomass burning and urban air pollution over the Central Mexican Plateau, Atmospheric Chemistry and Physics, 9, 4929–4944, 2009.

de Foy, B.: City-level variations in NOx emissions derived from hourly monitoring data in Chicago, Atmospheric Environment, 176, 128–139, 2018.

Demetillo, M. A. G., Harkins, C., McDonald, B. C., Chodrow, P. S., Sun, K., and Pusede, S. E.: Space-Based Observational Constraints on NO2 Air Pollution Inequality From Diesel Traffic in Major US Cities, Geophysical Research Letters, 48, e2021GL094 333, 2021.

Demuzere, M., Kittner, J., Martilli, A., Mills, G., Moede, C., Stewart, I. D., van Vliet, J., and Bechtel, B.: A global map of Local Climate Zones to support earth system modelling and urban scale environmental science, Earth System Science Data Discussions, pp. 1–57, 2022.

Djuricin, S., Pataki, D. E., and Xu, X.: A comparison of tracer methods for quantifying CO_2 sources in an urban region, Journal of Geophysical Research Atmospheres, 115, https://doi.org/10.1029/2009JD012236, 2010.

Duncan, B. N., Lamsal, L. N., Thompson, A. M., Yoshida, Y., Lu, Z., Streets, D. G., Hurwitz, M. M., and Pickering, K. E.: A space-based, high-resolution view of notable changes in urban NOx pollution around the world (2005–2014), Journal of Geophysical Research: Atmospheres, 121, 976–996, 2016.

Eldering, A.: OCO-3 B10 QTS Evaluation XCO2 Lite Files, https://doi.org/10.22002/D1.2046, 2021.

Eldering, A., Taylor, T. E., O'Dell, C. W., and Pavlick, R.: The OCO-3 mission: measurement objectives and expected performance based on 1 year of simulated data, Atmospheric Measurement Techniques, 12, 2341–2370, 2019.

Famulari, D., Nemitz, E., Di Marco, C., Phillips, G. J., Thomas, R., House, E., and Fowler, D.: Eddy-covariance measurements of nitrous oxide fluxes above a city, Agricultural and forest meteorology, 150, 786–793, 2010.

Fasoli, B., Lin, J. C., Bowling, D. R., Mitchell, L., and Mendoza, D.: Simulating atmospheric tracer concentrations for spatially distributed receptors: updates to the Stochastic Time-Inverted Lagrangian Transport model's R interface (STILT-R version 2), Geoscientific Model Development, 11, 2813–2824, 2018.

Fujinawa, T., Kuze, A., Suto, H., Shiomi, K., Kanaya, Y., Kawashima, T., Kataoka, F., Mori, S., Eskes, H., and Tanimoto, H.: First concurrent observations of NO2 and CO2 from power plant plumes by airborne remote sensing, Geophysical Research Letters, 48, e2021GL092 685, 2021.

Ghasemifard, H., Vogel, F. R., Yuan, Y., Luepke, M., Chen, J., Ries, L., Leuchner, M., Schunk, C., Noreen Vardag, S., and Menzel, A.: Pollution events at the high-altitude mountain site Zugspitze-Schneefernerhaus (2670 m asl), Germany, Atmosphere, 10, 330, 2019.

Gonzalez, A., Millet, D. B., Yu, X., Wells, K. C., Griffis, T. J., Baier, B. C., Campbell, P. C., Choi, Y., DiGangi, J. P., Gvakharia, A., et al.: Fossil Versus Nonfossil CO Sources in the US: New Airborne Constraints From ACT-America and GEM, Geophysical Research Letters, 48, e2021GL093 361, 2021.

Gurney, K. R., Patarasuk, R., Liang, J., Song, Y., O'Keeffe, D., Rao, P., Whetstone, J. R., Duren, R. M., Eldering, A., and Miller, C.: The Hestia fossil fuel CO_2 emissions data product for the Los Angeles megacity (Hestia-LA), Earth System Science Data, 11, 1309–1335, https://doi.org/10.5194/essd-11-1309-2019, 2019.

Hakkarainen, J., Szelag, M. E., Ialongo, I., Retscher, C., Oda, T., and Crisp, D.: Analyzing nitrogen oxides to carbon dioxide emission ratios from space: A case study of Matimba Power Station in South Africa, Atmospheric Environment: X, p. 100110, https://doi.org/10.1016/j.aeaoa.2021.100110, 2021.

Han, S., Kondo, Y., Oshima, N., Takegawa, N., Miyazaki, Y., Hu, M., Lin, P., Deng, Z., Zhao, Y., Sugimoto, N., et al.: Temporal variations of elemental carbon in Beijing, Journal of Geophysical Research: Atmospheres, 114, 2009.

Harrison, R. M., Dall'Osto, M., Beddows, D., Thorpe, A. J., Bloss, W. J., Allan, J. D., Coe, H., Dorsey, J. R., Gallagher, M., Martin, C., et al.: Atmospheric chemistry and physics in the atmosphere of a developed megacity (London): an overview of the REPARTEE experiment and its conclusions, Atmospheric Chemistry and Physics, 12, 3065–3114, 2012.

Haszpra, L., Ferenczi, Z., and Barcza, Z.: Estimation of greenhouse gas emission factors based on observed covariance of CO_2 , CH_4 , N2O and CO mole fractions, Environmental Sciences Europe, 31, https://doi.org/10.1186/s12302-019-0277-y, 2019.

Hedelius, J. K., Viatte, C., Wunch, D., Roehl, C. M., Toon, G. C., Chen, J., Jones, T., Wofsy, S. C., Franklin, J. E., Parker, H., Dubey, M. K., and Wennberg, P. O.: Assessment of errors and biases in retrievals of XCO_2 , XCH_4 , XCO, and XN2O from a 0.5 cm-1 resolution solar-viewing spectrometer, Atmospheric Measurement Techniques, 9, 3527–3546, https://doi.org/10.5194/amt-9-3527-2016, 2016.

Hedelius, J. K., Liu, J., Oda, T., Maksyutov, S., Roehl, C. M., Iraci, L. T., Podolske, J. R., Hillyard, P. W., Liang, J., Gurney, K. R., Wunch, D., and Wennberg, P. O.: Southern California megacity CO_2 , CH_4 , and CO flux estimates using ground-and space-based remote sensing and a Lagrangian model, Atmospheric Chemistry and Physics, 18, 16 271–16 291, https://doi.org/10.5194/acp-18-16271-2018, 2018.

Huang, X., Wang, T., Talbot, R., Xie, M., Mao, H., Li, S., Zhuang, B., Yang, X., Fu, C., Zhu, J., et al.: Temporal characteristics of atmospheric CO2 in urban Nanjing, China, Atmospheric Research, 153, 437–450, 2015.

Hudman, R. C., Murray, L. T., Jacob, D. J., Millet, D., Turquety, S., Wu, S., Blake, D., Goldstein, A., Holloway, J., and Sachse, G. W.: Biogenic versus anthropogenic sources of CO in the United States, Geophysical Research Letters, 35, 2008.

Kaiser, J., Heil, A., Andreae, M., Benedetti, A., Chubarova, N., Jones, L., Morcrette, J.-J., Razinger, M., Schultz, M., Suttie, M., et al.: Biomass burning emissions estimated with a global fire assimilation system based on observed fire radiative power, Biogeosciences, 9, 527–554, 2012.

Kerr, G. H., Goldberg, D. L., and Anenberg, S. C.: COVID-19 pandemic reveals persistent disparities in nitrogen dioxide pollution, Proceedings of the National Academy of Sciences, 118, 2021.

Kiel, M., Eldering, A., Roten, D. D., Lin, J. C., Feng, S., Lei, R., Lauvaux, T., Oda, T., Roehl, C. M., Blavier, J.-F., et al.: Urban-focused satellite CO2 observations from the Orbiting Carbon Observatory-3: A first look at the Los Angeles megacity, Remote Sensing of Environment, 258, 112 314, 2021.

Lama, S., Houweling, S., Boersma, K. F., Eskes, H., Aben, I., Gon, H. A. C. D. V. D., Krol, M. C., Dolman, H., Borsdorff, T., and Lorente, A.: Quantifying burning efficiency in megacities using the NO_2 :CO ratio from the Tropospheric Monitoring Instrument (TROPOMI), Atmospheric Chemistry and Physics, 20, 10 295–10 310, https://doi.org/10.5194/acp-20-10295-2020, 2020.

Laughner, J. L., Neu, J. L., Schimel, D., Wennberg, P. O., Barsanti, K., Bowman, K. W., Chatterjee, A., Croes, B. E., Fitzmaurice, H. L., Henze, D. K., et al.: Societal shifts due to COVID-19 reveal large-scale complexities and feedbacks between atmospheric chemistry and climate change, Proceedings of the National Academy of Sciences, 118, 2021.

Lei, R., Feng, S., Danjou, A., Broquet, G., Wu, D., Lin, J. C., O'Dell, C. W., and Lauvaux, T.: Fossil fuel CO2 emissions over metropolitan areas from space: A multi-model analysis of OCO-2 data over Lahore, Pakistan, Remote Sensing of Environment, 264, 112 625, 2021.

Lin, J. and Gerbig, C.: Accounting for the effect of transport errors on tracer inversions, Geophysical Research Letters, 32, 2005.

Lin, J., Gerbig, C., Wofsy, S., Andrews, A., Daube, B., Davis, K., and Grainger, C.: A near-field tool for simulating the upstream influence of atmospheric observations: The Stochastic Time-Inverted Lagrangian Transport (STILT) model, Journal of Geophysical Research: Atmospheres, 108, 2003.

Lin, J. C., Mitchell, L., Crosman, E., Mendoza, D. L., Buchert, M., Bares, R., Fasoli, B., Bowling, D. R., Pataki, D., Catharine, D., Strong, C., Gurney, K. R., Patarasuk, R., Baasandorj, M., Jacques, A., Hoch, S., Horel, J., and Ehleringer, J.: CO_2 and carbon emissions from cities linkages to air quality, socioeconomic activity, and stakeholders in the Salt Lake city urban area, Bulletin of the American Meteorological Society, 99, 2325–2339, https://doi.org/10.1175/BAMS-D-17-0037.1, 2018.

Lin, J. C., Bares, R., Fasoli, B., Garcia, M., Crosman, E., and Lyman, S.: Declining methane emissions and steady, high leakage rates observed over multiple years in a western US oil/gas production basin, Scientific reports, 11, 1–12, 2021.

Lindenmaier, R., Dubey, M. K., Henderson, B. G., Butterfield, Z. T., Herman, J. R., Rahn, T., and Lee, S. H.: Multiscale observations of CO_2 , $^{13}CO_2$, and pollutants at Four Corners for emission verification and attribution, Proceedings of the National Academy of Sciences of the United States of America, 111, 8386–8391, https://doi.org/10.1073/pnas.1321883111, 2014.

Lopez, M., Schmidt, M., Delmotte, M., Colomb, A., Gros, V., Janssen, C., Lehman, S. J., Mondelain, D., Perrussel, O., Ramonet, M., Xueref-Remy, I., and Bousquet, P.: CO, NOx and $13CO_2$ as tracers for fossil fuel CO_2 : Results from a pilot study in Paris during winter 2010, Atmospheric Chemistry and Physics, 13, 7343–7358, https://doi.org/10.5194/acp-13-7343-2013, 2013.

Makarova, M. V., Alberti, C., Ionov, D. V., Hase, F., Foka, S. C., Blumenstock, T., Warneke, T., Virolainen, Y. A., Kostsov, V. S., Frey, M., Poberovskii, A. V., Timofeyev, Y. M., Paramonova, N. N., Volkova, K. A., Zaitsev, N. A., Biryukov, E. Y., Osipov, S. I., Makarov, B. K., Polyakov, A. V., Ivakhov, V. M., Imhasin, H. K., and Mikhailov, E. F.: Emission Monitoring Mobile Experiment (EMME): An overview and first results of the St. Petersburg megacity campaign 2019, Atmospheric Measurement Techniques, 14, 1047–1073, https://doi.org/10.5194/amt-14-1047-2021, 2021.

Miller, S. M., Matross, D. M., Andrews, A. E., Millet, D. B., Longo, M., Gottlieb, E. W., Hirsch, A. I., Gerbig, C., Lin, J. C., Daube, B. C., et al.: Sources of carbon monoxide and formaldehyde in North America determined from high-resolution atmospheric data, Atmospheric Chemistry and Physics, 8, 7673–7696, 2008.

Mitchell, L. E., Lin, J. C., Bowling, D. R., Pataki, D. E., Strong, C., Schauer, A. J., Bares, R., Bush, S. E., Stephens, B. B., Mendoza, D., et al.: Long-term urban carbon dioxide observations reveal spatial and temporal dynamics related to urban characteristics and growth, Proceedings of the National Academy of Sciences, 115, 2912–2917, 2018.

Moldanová, J., Fridell, E., Popovicheva, O., Demirdjian, B., Tishkova, V., Faccinetto, A., and Focsa, C.: Characterisation of particulate matter and gaseous emissions from a large ship diesel engine, Atmospheric Environment, 43, 2632–2641, 2009.

Nathan, B., Lauvaux, T., Turnbull, J., and Gurney, K.: Investigations into the use of multi-species measurements for source apportionment of the Indianapolis fossil fuel CO_2 signal, Elementa, 6, https://doi.org/10.1525/elementa.131, 2018.

O'Shea, S. J., Allen, G., Fleming, Z. L., Bauguitte, S. J.-B., Percival, C. J., Gallagher, M. W., Lee, J., Helfter, C., and Nemitz, E.: Area fluxes of carbon dioxide, methane, and carbon monoxide derived from airborne measurements around Greater London: A case study during summer 2012, Journal of Geophysical Research: Atmospheres, 119, 4940–4952, 2014.

Palmer, P. I., Suntharalingam, P., Jones, D. B., Jacob, D. J., Streets, D. G., Fu, Q., Vay, S. A., and Sachse, G. W.: Using CO_2 : CO correlations to improve inverse analyses of carbon fluxes, Journal of Geophysical Research Atmospheres, 111, https://doi.org/10.1029/2005JD006697, 2006.

Park, H., Jeong, S., Park, H., Labzovskii, L. D., and Bowman, K. W.: An assessment of emission characteristics of Northern Hemisphere cities using spaceborne observations of CO_2 , CO, and NO_2 , Remote Sensing of Environment, 254, https://doi.org/10.1016/j.rse.2020.112246, 2021.

Pitt, J. R., Allen, G., Bauguitte, S. J.-B., Gallagher, M. W., Lee, J. D., Drysdale, W., Nelson, B., Manning, A. J., and Palmer, P. I.: Assessing London CO2, CH4 and CO emissions using aircraft measurements and dispersion modelling, Atmospheric Chemistry and Physics, 19, 8931–8945, 2019.

Plant, G., Kort, E. A., Floerchinger, C., Gvakharia, A., Vimont, I., and Sweeney, C.: Large fugitive methane emissions from urban centers along the US East Coast, Geophysical research letters, 46, 8500–8507, 2019.

Popa, M. E., Vollmer, M. K., Jordan, A., Brand, W. A., Pathirana, S. L., Rothe, M., and Röckmann, T.: Vehicle emissions of greenhouse gases and related tracers from a tunnel study: CO : CO_2 , N2O : CH_4 : O2 : Atios, and the stable isotopes 13C and 18O in CO_2 and CO, Atmospheric Chemistry and Physics, 14, 2105–2123, https://doi.org/10.5194/acp-14-2105-2014, 2014.

Reuter, M., Buchwitz, M., Schneising, O., Krautwurst, S., O'Dell, C. W., Richter, A., Bovensmann, H., and Burrows, J. P.: Towards monitoring localized CO_2 emissions from space: Co-located regional CO_2 and NO_2 enhancements observed by the OCO-2 and S5P satellites, Atmospheric Chemistry and Physics, 19, 9371–9383, https://doi.org/10.5194/acp-19-9371-2019, 2019.

Schneising, O., Buchwitz, M., Reuter, M., Bovensmann, H., Burrows, J. P., Borsdorff, T., Deutscher, N. M., Feist, D. G., Griffith, D. W., Hase, F., et al.: A scientific algorithm to simultaneously retrieve carbon monoxide and methane from TROPOMI onboard Sentinel-5 Precursor, Atmospheric Measurement Techniques, 12, 6771–6802, 2019.

Schuh, A. E., Otte, M., Lauvaux, T., and Oda, T.: Far-field biogenic and anthropogenic emissions as a dominant source of variability in local urban carbon budgets: A global high-resolution model study with implications for satellite remote sensing, Remote Sensing of Environment, 262, 112 473, 2021.

Shekhar, A., Chen, J., Paetzold, J. C., Dietrich, F., Zhao, X., Bhattacharjee, S., Ruisinger, V., and Wofsy, S. C.: Anthropogenic CO2 emissions assessment of Nile Delta using XCO2 and SIF data from OCO-2 satellite, Environmental Research Letters, 15, 095 010, 2020.

Silva, S. and Arellano, A.: Characterizing Regional-Scale Combustion Using Satellite Retrievals of CO, NO_2 and CO_2 , Remote Sensing, 9, 744, https://doi.org/10.3390/rs9070744, 2017.

Silva, S. J., Arellano, A. F., and Worden, H. M.: Toward anthropogenic combustion emission constraints from space-based analysis of urban CO_2 /CO sensitivity, Geophysical Research Letters, 40, 4971–4976, https://doi.org/10.1002/grl.50954, 2013.

Sim, S., Jeong, S., Park, H., Park, C., Kwak, K. H., Lee, S. B., Kim, C. H., Lee, S., Chang, J. S., Kang, H., and Woo, J. H.: Co-benefit potential of urban CO_2 and air quality monitoring: A study on the first mobile campaign and building monitoring experiments in Seoul during the winter, Atmospheric Pollution Research, 11, 1963–1970, https://doi.org/10.1016/j.apr.2020.08.009, 2020.

Solazzo, E., Crippa, M., Guizzardi, D., Muntean, M., Choulga, M., and Janssens-Maenhout, G.: Uncertainties in the Emissions Database for Global Atmospheric Research (EDGAR) emission inventory of greenhouse gases, Atmospheric Chemistry and Physics, 21, 5655–5683, https://doi.org/10.5194/acp-21-5655-2021, 2021.

Stewart, I. D. and Oke, T. R.: Local climate zones for urban temperature studies, Bulletin of the American Meteorological Society, 93, 1879–1900, 2012.

Super, I., van der Gon, H. A. D., Visschedijk, A. J., Moerman, M. M., Chen, H., van der Molen, M. K., and Peters, W.: Interpreting continuous in-situ observations of carbon dioxide and carbon monoxide in the urban port area of Rotterdam, Atmospheric Pollution Research, 8, 174–187, https://doi.org/10.1016/j.apr.2016.08.008, 2017.

Surl, L., Palmer, P. I., and González Abad, G.: Which processes drive observed variations of HCHO columns over India?, Atmospheric Chemistry and Physics, 18, 4549–4566, 2018.

Tang, W., Arellano, A. F., DiGangi, J. P., Choi, Y., Diskin, G. S., Agustí-Panareda, A., Parrington, M., Massart, S., Gaubert, B., Lee, Y., et al.: Evaluating high-resolution forecasts of atmospheric CO and CO 2 from a global prediction system during KORUS-AQ field campaign, Atmospheric Chemistry and Physics, 18, 11 007–11 030, 2018.

Tang, W., Gaubert, B., Emmons, L., Choi, Y., DiGangi, J., Diskin, G., Xu, X., He, C., Worden, H., Tilmes, S., Buchholz, R., Halliday, H., and Arellano, A.: On the relationship between tropospheric CO and CO_2 during KORUS-AQ and its role in constraining anthropogenic CO_2 , Atmospheric Chemistry and Physics, pp. 1–53, https://doi.org/10.5194/acp-2020-864, 2020.

Taylor, T. E., Eldering, A., Merrelli, A., Kiel, M., Somkuti, P., Cheng, C., Rosenberg, R., Fisher, B., Crisp, D., Basilio, R., et al.: OCO-3 early mission operations and initial (vEarly) XCO2 and SIF retrievals, Remote Sensing of Environment, 251, 112 032, 2020.

Turnbull, J., Karion, A., Fischer, M., Faloona, I., Guilderson, T., Lehman, S., Miller, B., Miller, J., Montzka, S., Sherwood, T., et al.: Assessment of fossil fuel carbon dioxide and other anthropogenic trace gas emissions from airborne measurements over Sacramento, California in spring 2009, Atmospheric Chemistry and Physics, 11, 705–721, 2011a.

Turnbull, J. C., Tans, P. P., Lehman, S. J., Baker, D., Conway, T. J., Chung, Y. S., Gregg, J., Miller, J. B., Southon, J. R., and Zhou, L. X.: Atmospheric observations of carbon monoxide and fossil fuel CO_2 emissions from East Asia, Journal of Geophysical Research Atmospheres, 116, https://doi.org/10.1029/2011JD016691, 2011b.

Turnbull, J. C., Sweeney, C., Karion, A., Newberger, T., Lehman, S. J., Tans, P. P., Davis, K. J., Lauvaux, T., Miles, N. L., Richardson, S. J., et al.: Toward quantification and source sector identification of fossil fuel CO2 emissions from an urban area: Results from the INFLUX experiment, Journal of Geophysical Research: Atmospheres, 120, 292–312, 2015.

Turner, A. J., Köhler, P., Magney, T. S., Frankenberg, C., Fung, I., and Cohen, R. C.: A double peak in the seasonality of California's photosynthesis as observed from space, Biogeosciences, 17, 405–422, 2020.

Veefkind, J., Aben, I., McMullan, K., Förster, H., De Vries, J., Otter, G., Claas, J., Eskes, H., De Haan, J., Kleipool, Q., et al.: TROPOMI on the ESA Sentinel-5 Precursor: A GMES mission for global observations of the atmospheric composition for climate, air quality and ozone layer applications, Remote sensing of environment, 120, 70–83, 2012.

Venables, W. N. and Ripley, B. D.: Modern Applied Statistics with S, Springer, New York, fourth edn., http://www.stats.ox.ac.uk/pub/MASS4, iSBN 0-387-95457-0, 2002.

Vollmer, M. K., Juergens, N., Steinbacher, M., Reimann, S., Weilenmann, M., and Buchmann, B.: Road vehicle emissions of molecular hydrogen (H2) from a tunnel study, Atmospheric Environment, 41, 8355–8369, 2007.

Wang, H., Jacob, D. J., Kopacz, M., Jones, D. B. A., Suntharalingam, P., Fisher, J. A., Nassar, R., Pawson, S., and Nielsen, J. E.: Atmospheric Chemistry and Physics Error correlation between CO_2 and CO as constraint for CO_2 flux inversions using satellite data, Atmos. Chem. Phys, 9, 7313–7323, www.atmos-chem-phys.net/9/7313/2009/, 2009.

Wang, X., Lei, Y., Yan, L., Liu, T., Zhang, Q., and He, K.: A unit-based emission inventory of SO2, NOx and PM for the Chinese iron and steel industry from 2010 to 2015, Science of the total environment, 676, 18–30, 2019.

Wang, Y., Munger, J. W., Xu, S., McElroy, M. B., Hao, J., Nielsen, C. P., and Ma, H.: CO_2 and its correlation with CO at a rural site near Beijing: Implications for combustion efficiency in China, Atmospheric Chemistry and Physics, 10, 8881–8897, https://doi.org/10.5194/acp-10-8881-2010, 2010.

Wennberg, P. O., Mui, W., Wunch, D., Kort, E. A., Blake, D. R., Atlas, E. L., Santoni, G. W., Wofsy, S. C., Diskin, G. S., Jeong, S., et al.: On the sources of methane to the Los Angeles atmosphere, Environmental science & technology, 46, 9282–9289, 2012.

Wennberg, P. O., Wunch, D., Roehl, C., Blavier, J.-F., Toon, G. C., and Allen, N.: TCCON data from Caltech (US), Release GGG2020R0, TCCON data archive, hosted by CaltechDATA, https://doi.org/10.14291/tccon.ggg2020.pasadena01.R0, 2017.

Westerdahl, D., Wang, X., Pan, X., and Zhang, K. M.: Characterization of on-road vehicle emission factors and microenvironmental air quality in Beijing, China, Atmospheric Environment, 43, 697–705, 2009.

Williams, E., Lerner, B., Murphy, P., Herndon, S., and Zahniser, M.: Emissions of NOx, SO2, CO, and HCHO from commercial marine shipping during Texas Air Quality Study (TexAQS) 2006, Journal of Geophysical Research: Atmospheres, 114, 2009.

Wu, D., Lin, J. C., Fasoli, B., Oda, T., Ye, X., Lauvaux, T., Yang, E. G., and Kort, E. A.: A Lagrangian approach towards extracting signals of urban CO 2 emissions from satellite observations of atmospheric column CO 2 (XCO 2): X-Stochastic Time-Inverted Lagrangian Transport model ("X-STILT v1"), Geoscientific Model Development, 11, 4843–4871, 2018.

Wu, D., Lin, J. C., Oda, T., and Kort, E. A.: Space-based quantification of per capita CO2 emissions from cities, Environmental Research Letters, 15, 035 004, 2020.

Wu, D., Lin, J. C., Duarte, H. F., Yadav, V., Parazoo, N. C., Oda, T., and Kort, E. A.: A model for urban biogenic CO2 fluxes: Solar-Induced Fluorescence for Modeling Urban biogenic Fluxes (SMUrF v1), Geoscientific Model Development, 14, 3633–3661, 2021.

Wunch, D., Wennberg, P., Toon, G., Keppel-Aleks, G., and Yavin, Y.: Emissions of greenhouse gases from a North American megacity, Geophysical research letters, 36, 2009.

Xia, L., Zhang, G., Liu, L., Li, B., Zhan, M., Kong, P., and Wang, H.: Atmospheric CO2 and CO at Jingdezhen station in central China: Understanding the regional transport and combustion efficiency, Atmospheric Environment, 222, 117 104, 2020.

Ye, X., Lauvaux, T., Kort, E. A., Oda, T., Feng, S., Lin, J. C., Yang, E. G., and Wu, D.: Constraining Fossil Fuel CO2 Emissions From Urban Area Using OCO-2 Observations of Total Column CO2, Journal of Geophysical Research: Atmospheres, 125, e2019JD030 528, 2020.

Yokota, T., Yoshida, Y., Eguchi, N., Ota, Y., Tanaka, T., Watanabe, H., and Maksyutov, S.: Global concentrations of CO2 and CH4 retrieved from GOSAT: First preliminary results, Sola, 5, 160–163, 2009.

Yuan, L. and Smith, A. C.: CO and CO2 emissions from spontaneous heating of coal under different ventilation rates, International Journal of Coal Geology, 88, 24–30, 2011.

Zhang, F., Chen, Y., Tian, C., Lou, D., Li, J., Zhang, G., and Matthias, V.: Emission factors for gaseous and particulate pollutants from offshore diesel engine vessels in China, Atmospheric Chemistry and Physics, 16, 6319–6334, 2016.

Zhang, Y., Smith, S. J., Bowden, J. H., Adelman, Z., and West, J. J.: Co-benefits of global, domestic, and sectoral greenhouse gas mitigation for US air quality and human health in 2050, Environmental Research Letters, 12, 114 033, 2017.

Zhang, Y., Joiner, J., Alemohammad, S. H., Zhou, S., and Gentine, P.: A global spatially contiguous solar-induced fluorescence (CSIF) dataset using neural networks, Biogeosciences, 15, 5779–5800, 2018.

Zhu, L., Jacob, D. J., Mickley, L. J., Marais, E. A., Cohan, D. S., Yoshida, Y., Duncan, B. N., Abad, G. G., and Chance, K. V.: Anthropogenic emissions of highly reactive volatile organic compounds in eastern Texas inferred from oversampling of satellite (OMI) measurements of HCHO columns, Environmental Research Letters, 9, 114 004, 2014.